



## Calhoun: The NPS Institutional Archive DSpace Repository

---

Theses and Dissertations

1. Thesis and Dissertation Collection, all items

---

1991-12

### Focusing transition radiation with cylindrical and elliptical optics

Votruba, Paul Matthew

Monterey, California. Naval Postgraduate School

---

<http://hdl.handle.net/10945/28226>

---

*Downloaded from NPS Archive: Calhoun*



<http://www.nps.edu/library>

Calhoun is the Naval Postgraduate School's public access digital repository for research materials and institutional publications created by the NPS community.

Calhoun is named for Professor of Mathematics Guy K. Calhoun, NPS's first appointed -- and published -- scholarly author.

Dudley Knox Library / Naval Postgraduate School  
411 Dyer Road / 1 University Circle  
Monterey, California USA 93943









# NAVAL POSTGRADUATE SCHOOL

## Monterey, California



# THEESIS

FOCUSING X-RAY TRANSITION RADIATION  
WITH CYLINDRICAL AND ELLIPTICAL OPTICS

by

Paul Matthew Votruba

Thesis Advisor:

Xavier K. Maruyama

Approved for public release  
distribution unlimited.



Form Approved  
OMB No 0704-0188

## REPORT DOCUMENTATION PAGE

1a REPORT SECURITY CLASSIFICATION <b>Unclassified</b>		1b RESTRICTIVE MARKINGS	
2a SECURITY CLASSIFICATION AUTHORITY		3 DISTRIBUTION/AVAILABILITY OF REPORT <b>Approved for public release; distribution is unlimited.</b>	
2b DECLASSIFICATION/DOWNGRADING SCHEDULE		5 MONITORING ORGANIZATION REPORT NUMBER(S)	
4 PERFORMING ORGANIZATION REPORT NUMBER(S)			
6a NAME OF PERFORMING ORGANIZATION <b>Naval Postgraduate School</b>	6b OFFICE SYMBOL (If applicable) <b>33</b>	7a NAME OF MONITORING ORGANIZATION <b>Naval Postgraduate School</b>	
6c ADDRESS (City, State, and ZIP Code) <b>Monterey, CA 93943-5000</b>		7b ADDRESS (City, State, and ZIP Code) <b>Monterey, CA 93943-5000</b>	
8a NAME OF FUNDING/SPONSORING ORGANIZATION	8b OFFICE SYMBOL (If applicable)	9 PROCUREMENT INSTRUMENT IDENTIFICATION NUMBER	
8c ADDRESS (City, State, and ZIP Code)		10 SOURCE OF FUNDING NUMBERS	
		PROGRAM ELEMENT NO	PROJECT NO
		TASK NO	WORK UNIT ACCESSION NO
11 TITLE (Include Security Classification) <b>FOCUSING X-RAY TRANSITION RADIATION WITH CYLINDRICAL AND ELLIPTICAL OPTICS</b>			
12 PERSONAL AUTHOR(S) <b>Votruba, Paul M.</b>			
13a TYPE OF REPORT <b>Master's Thesis</b>	13b TIME COVERED FROM _____ TO _____	14 DATE OF REPORT (Year, Month, Day) <b>December 1991</b>	15 PAGE COUNT <b>99</b>
16 SUPPLEMENTARY NOTATION <b>The views expressed in this thesis are those of the author and do not reflect the official policy or position of the Department of Defense or the U.S. Government.</b>			
17 COSATI CODES		18 SUBJECT TERMS (Continue on reverse if necessary and identify by block number) <b>Focusing Optics, Transition Radiation, X-Rays</b>	
19 ABSTRACT (Continue on reverse if necessary and identify by block number)  <b>We have demonstrated the ability of a nickel elliptical tube to focus the conically diverging pattern of x-ray transition radiation. The x-ray TR was produced by passing moderate-energy (60 to 100 MeV) electron beams through targets consisting of thin (<math>1 \mu m</math>) multiple foils of aluminum and titanium. The foils were placed in a vacuum chamber, perpendicular to the Naval Postgraduate School's linac primary beamline. An elliptical nickel tube, with a length of 30.5 cm, was placed concentric to the axis of the conical photon beam (as defined by the axis of the electron beam) with an entrance and exit of 1.4 m and 1.7 m, respectively, from the source of the TR at the end of the foil stack. The intensity profile was subsequently measured with a linear image detector placed 3.0 m from the exit of the foil stack. Through a series of experiments, taking into account the effects of surface roughness, the</b>			
20 DISTRIBUTION/AVAILABILITY OF ABSTRACT <input checked="" type="checkbox"/> UNCLASSIFIED/UNLIMITED <input type="checkbox"/> SAME AS RPT		21 ABSTRACT SECURITY CLASSIFICATION <b>Unclassified</b>	
22a NAME OF RESPONSIBLE INDIVIDUAL <b>Xavier K. Maruyama</b>		22b TELEPHONE (Include Area Code) <b>(408) 646-2431</b>	22c OFFICE SYMBOL <b>Ph/Mx</b>

UNCLASSIFIED

SECURITY CLASSIFICATION OF THIS PAGE

Block 19 Continued

nickel elliptical tube demonstrated the ability to collect 3 to 5 times more energy than a cylindrical quartz tube.

Approved for public release; distribution is unlimited.

Focusing Transition Radiation with  
Cylindrical and Elliptical Optics

by

Paul M. Votruba  
Lieutenant, United States Navy  
B.S., University of Minnesota, 1982

Submitted in partial fulfillment of the  
requirements for the degree of

MASTERS OF SCIENCE IN PHYSICS

from the

NAVAL POSTGRADUATE SCHOOL  
December 1991

## ABSTRACT

We have demonstrated the ability of a nickel elliptical tube to focus the conically diverging pattern of x-ray transition radiation. The x-ray TR was produced by passing moderate-energy (60 to 100 MeV) electron beams through targets consisting of thin ( $1 \mu\text{m}$ ) multiple foils of aluminum and titanium. The foils were placed in a vacuum chamber; perpendicular to the Naval Postgraduate School's linac primary beamline. An elliptical nickel tube, with a length of 30.5 cm, was placed concentric to the axis of the conical photon beam (as defined by the axis of the electron beam) with an entrance and exit of 1.4 m and 1.7 m, respectively, from the source of the TR at the end of the foil stack. The intensity profile was subsequently measured with a linear image detector placed 3.0 m from the exit of the foil stack. Through a series of experiments, taking into account the effects of surface roughness, the nickel elliptical tube demonstrated the ability to collect 3 to 5 times more energy than a cylindrical quartz tube.

## TABLE OF CONTENTS

I.	INTRODUCTION . . . . .	1
A.	THE THEORY OF TRANSITION RADIATION . . . . .	1
B.	TRANSITION RADIATION AS A SOFT X-RAY SOURCE . .	6
II.	FOCUSING OPTICS . . . . .	7
A.	GRAZING INCIDENCE . . . . .	7
B.	DESIGN OF CYLINDRICAL OPTICS . . . . .	9
C.	CYLINDRICAL FOCUSING SIMULATION . . . . .	16
D.	ENERGY AND ANGULAR DEPENDANT REFLECTIVE LOSSES	16
E.	ELLIPTICAL OPTICS . . . . .	23
III.	EXPERIMENTAL SETUP AND PROCEDURE . . . . .	31
A.	LINAC . . . . .	31
B.	MAIN SCATTERING CHAMBER . . . . .	31
C.	DUMP MAGNET . . . . .	33
D.	FOCUSING OPTICS . . . . .	33
E.	LINEAR IMAGE SENSOR . . . . .	33
F.	ALIGNMENT . . . . .	34
IV.	RESULTS . . . . .	36
V.	ANALYSIS . . . . .	48
A.	OPTIC LOSSES . . . . .	48
B.	EFFECTS OF MYLAR . . . . .	65
VI.	CONCLUSIONS AND RECOMMENDATIONS . . . . .	78
	LIST OF REFERENCES . . . . .	80

APPENDIX A . . . . .	82
A. ALTERNATIVE X-RAY OPTICS . . . . .	82
INITIAL DISTRIBUTION LIST . . . . .	89

## ACKNOWLEDGEMENTS

I'd like to thank Professor X. K. Maruyama for providing me with the technical guidance required while doing my research. His support made this project a very worthwhile educational experience. Dr. M. A. Piestrup, the real driving force behind my experiment, deserves special recognition. If it weren't for his design of an elliptical optic, along with the idea of coupling it to a Transition Radiation source, this experiment would not have taken place.

Charles Gray and Jack Harris, the men I conducted the experiment with, are true professionals. In addition, their friendship during the course of the experiment created a very enjoyable atmosphere. Adrian Ho provided me technical insight during the analysis of my data. His time and efforts are greatly appreciated. Mr. Don Snyder and Mr. Harold Reitdyk operate and maintain the linac, thus making it possible to conduct experiments in a timely manner.

I had special assistance from two of my closest friends, Major Thomas Schwendtner and Captain Drew Dwyer. Utilizing their computer expertise, these two men made the analysis of my data possible. Their friendship and assistance will always be remembered.

I'd especially like to thank my wife Cheryl. Her support and understanding throughout my time in the Navy and especially during my tour at the Naval Postgraduate School made the completion of this thesis a reality. Finally, I'd like to thank my father for providing me with the guidance in my life that enabled me to face this challenge. This work is dedicated to him.

## I. INTRODUCTION

### A. THE THEORY OF TRANSITION RADIATION

Transition radiation was discovered by Ginsburg and Frank in 1946 [Ref. 1]. They noted this radiation whenever a charged particle suddenly passed from one medium to another. Since different media have different electromagnetic properties, the fields characteristic of the particle's motion will also be different. This will be true even if the particle's motion is uniform throughout both media. The fields must reorganize as the particle passes through the interface of the media. During this reorganization, pieces of the fields are emitted as transition radiation.

When high energy electrons cross an interface between two media, transition radiation is produced in the form of soft x-rays. The yield of this radiation is proportional to the number of interfaces the electrons must cross. The interfaces under study and used in most applications are foil stacks separated by vacuum. Transition radiation is produced when the electrons cross the vacuum-foil interface. In order to maximize this photon production, the re-absorption of photons within the media must be minimized. The photon absorption in vacuum is negligible and in the foils is dependant upon the foil thickness. By making the foils as thin as possible, re-

absorption will be minimized. However, if the foil is less than a minimum thickness called the formation length, photon production will decrease significantly. Therefore, the optimum thickness of the foils which will balance photon production and re-absorption must be determined. In previous studies [Ref. 2] on soft x-ray transition radiation production, the foil thicknesses used have been between 0.5 and 5.0 microns.

Using thin foils of thickness  $l_2$  and plasma frequency  $\omega_2$  separated by a vacuum of thickness  $l_1$  and plasma frequency  $\omega_1$ , given  $l_1 \gg l_2$  and  $\omega_2 \gg \omega_1$ , the transition radiation is emitted at frequencies  $< \gamma\omega_1$  ( $\gamma = E/0.511$ , is the Lorentz factor where,  $E$  is the electron energy in MeV) [Ref. 3]. Above this frequency radiation falls off dramatically. Since the plasma frequency of a material is proportional to the square root of its density, and the above cutoff frequency is proportional to the plasma frequency, it follows that the cutoff frequency,  $\gamma\omega_p$ , is proportional to the square root of the foil density. The plasma frequency is given by [Ref. 4] to be:

$$\omega_p = \left( \frac{ve^2}{\epsilon_0 m} \right)^{1/2} \quad (1.1)$$

where  $n$  is the number of electrons in an individual foil and is determined by the foil density.

The spectral intensity produced by a single electron traversing a single foil interface is given by [Ref. 2] to be:

$$\frac{d^2N_o}{d\Omega d\omega} = \frac{\alpha \theta \omega}{16\pi^2 c^2} (Z_1 - Z_2) \quad (1.2)$$

where  $Z_1$  and  $Z_2$  are the formation lengths of the two dielectrics (media) given approximately by:

$$Z_i = \frac{c}{\omega \left( \frac{1}{\gamma^2} + \frac{\omega_i^2}{\omega^2} + \theta^2 \right)} \quad (1.3)$$

where  $i=1, 2$ ;  $\theta$  is the angle of emission with respect to the electron trajectory,  $\omega$  is the angular frequency of the radiation,  $\omega_i$  are the plasma frequencies of the dielectrics,  $\alpha$  is the fine structure constant ( $\alpha=1/137$ ),  $c$  is the speed of light,  $N_o$  is the number of generated x-ray photons,  $\Omega$  is the solid angle measured in steradians. If we neglect absorption and coherent phase addition, the total flux produced by  $M$  foils would be  $2Md^2N_o/d\Omega d\omega$ . However, the number of foils used is limited by re-absorption in the foils,  $M \leq 2\mu l_2$ , where  $\mu$  is the x-ray absorption coefficient and  $l_2$  is the thickness of the foil.

As can be seen in Figure 1, transition radiation is emitted in a very tight forward cone. The angle of peak emission is found by taking the derivative of equation 1.2 with respect to  $\theta$  and setting the expression equal to zero. This angle is given by [Ref. 2]:

$$\theta_p^2 = 1/3 \{ -(\delta_1 + \delta_2) + [(\delta_1 + \delta_2)^2 + 12\delta_1\delta_2]^{1/2} \} \quad (1.4)$$

where

$$\delta_i = \frac{1}{2\gamma^2} + \frac{\omega_i^2}{2\omega^2}, \quad i = 1, 2.$$

For  $\gamma \gg \frac{\omega}{\omega_i}$ , the angle of peak emission and the angular

width are approximated by:

$$\theta_p = \Delta\theta = \frac{1}{\gamma} \quad (1.5)$$

For example, assume a 50 MeV electron beam. The angle of peak emission,  $\theta_p$ , and the angular width,  $\Delta\theta$ , would be 10 mrad; therefore at one meter away from the foil stack, the radiation would illuminate an annulus of approximately  $3 \text{ cm}^2$ .

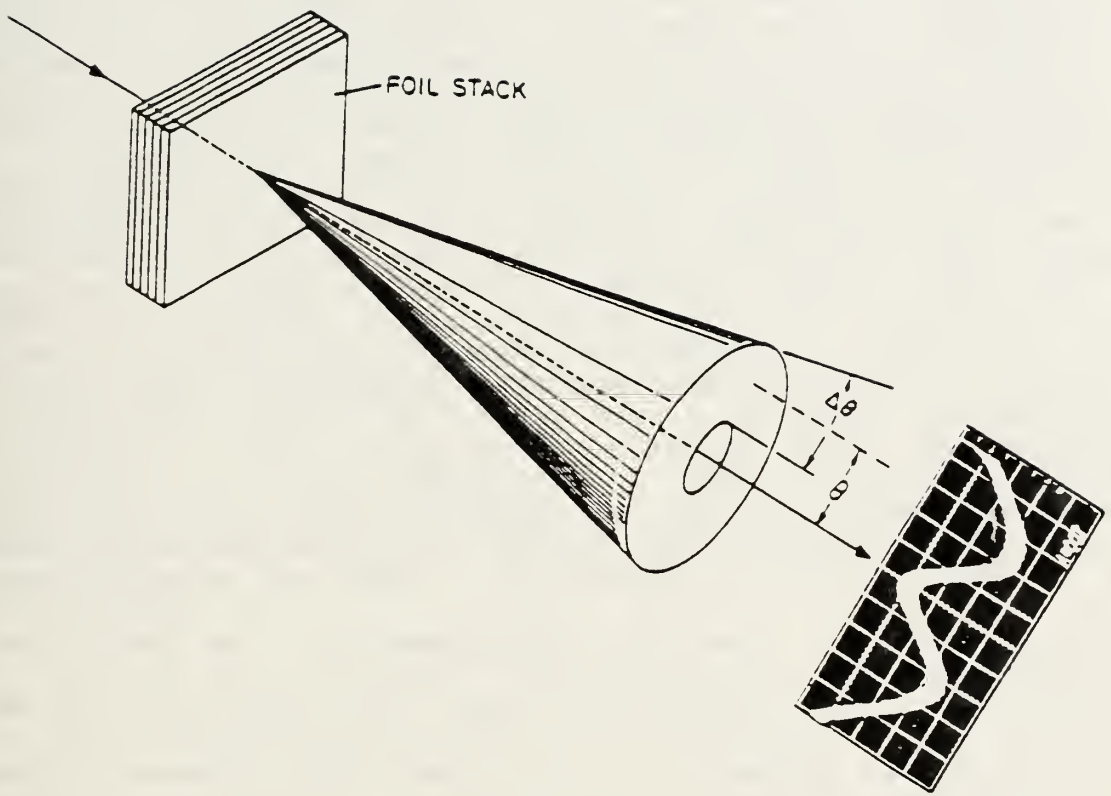


Figure 1. A schematic diagram of the cone of emission produced by transition radiation showing the peak emission angle and range of emission angles.

## B. TRANSITION RADIATION AS A SOFT X-RAY SOURCE

It has been shown in previous studies [Ref. 5] that transition radiation, TR, can provide a bright source of soft x-rays. One of the most attractive features of using TR as a source is that soft x-rays can be produced using moderate to low electron beam energies. It has been demonstrated [Ref. 6] that 900 eV to 3 keV soft x-rays can be generated by passing 17-109 MeV electron beams through targets consisting of thin multiple foil stacks. It follows that moderate energy linacs along with transition radiators can provide a practical alternative to high power soft x-ray production. When compared to synchrotron sources, transition radiation is brighter on a per electron basis by at least 3 orders of magnitude [Ref. 2, 7, 8]. In addition, due to the high energy of synchrotrons, in comparison to the low energy linacs required for TR, the cost advantages of the latter are substantial. As a matter of fact, the cost of a 50 MeV accelerator is competitive with conventional bremsstrahlung sources [Ref. 6].

## II. FOCUSING OPTICS

### A. GRAZING INCIDENCE

Grazing incidence optics have been used for many years in a wide variety of applications, ranging from x-ray microscopes to x-ray waveguides. In most cases, the reflecting optics are nothing more than cylindrical tubes with varying diameters. The inside surface of the tube is either straight or elliptical. However, the use of these simple optics has led to significant advances in the sciences. X-ray microscopes have been used to study biological specimens, while x-ray telescopes have been used to study the stars. In addition, the critical angle of reflection has been used in the design and fabrication of x-ray waveguides. These waveguides have demonstrated the ability to transmit soft x-rays an appreciable distance.

Due to the extremely tight conical and symmetrical pattern of transition radiation, it is well suited to the geometry involved with cylindrical grazing incidence optics. Since materials have an index of refraction less than unity at x-ray wavelengths, TR can be entirely reflected at a vacuum-material interface. The complex index of refraction,  $n$ , is given as:

$$n = 1 - \delta - i\beta$$

(2.1)

where  $\delta$  and  $\beta$  are positive, and  $\delta$  is defined in equation 1.4. If the imaginary part of the complex index of refraction,  $\beta$ , is negligible, total reflection from a vacuum-material interface occurs if the angle of incidence is less than the critical angle where:

$$\theta_c = \cos^{-1} (1 - \delta) = \frac{\omega_i}{\omega} \quad (2.2)$$

In equations 1.4 and 2.2,  $\omega_i$  is the plasma frequency of the optics medium and  $\omega$  is the frequency of the transition radiation [Ref. 9]. For purposes of this thesis, the angle of incidence (grazing angle) is defined as the angle between the reflecting optics surface and the incoming x-ray beam. The x-ray beam's angular divergence must be sufficiently small so that reflection of the x-ray beam occurs at the surface and is not absorbed. For a solid material, such as quartz, the maximum angle of incidence is given by the critical angle as previously stated.

For example, quartz has a plasma frequency of  $\omega_p = 33.2$  eV. This yields a critical angle  $\theta_c = 16.61$  mrad for 2 keV photons. Therefore x-rays hitting the surface of the optics at angles

less than 16.61 mrad will be reflected with almost 100% efficiency. The case is the same for conventional x-ray sources, however, due to the highly divergent nature of these sources, grazing incidence optics are impractical. Again, the main features of TR that make the geometry of a hollow cylindrical optic so perfect for focusing, is the small divergence and the circular symmetry around the axis defined by the electron beam. By placing a cylindrical optic so that the electron beam travels down the geometric center, the TR will be reflected and focused. Figures 2 and 3 illustrate the influence of cylindrical focusing optics on the TR x-ray emission profile by means of a computer ray tracing simulation.

#### B. DESIGN OF CYLINDRICAL OPTICS

Figure 4 shows the general design of the cylindrical optical focusing system. The dimensions that need to be specified are: the diameter of the cylindrical optic  $D$ , the location of the optic entrance  $L_1$ , the location of the optic exit  $L_2$ , and the location of the detector plane  $L_3$ . These dimensions must be designed in order to maximize the magnitude of the peak flux over a focal spot of specified diameter  $d_f$  for TR produced by an electron beam of diameter  $d_b$ . The first step is to determine the angle of peak emission of the TR.

This was previously determined and is given by equation 1.4. However, since the flux is emitted in an annulus, larger radial angles result in large areas of emission, and, hence, larger numbers of photons. In other words, more photons are emitted for angles slightly larger than  $\theta_p$ , because there is more area of emission. Therefore, this must be taken into account when designing the optics. The spectral intensity for a single interface is given by equation 1.2. In order to determine the optimum angle of emission, equation 1.2 is multiplied by  $\theta$ , the derivative with respect to  $\theta$  is taken, and the expression is set equal to zero. The optimum angle of emission for collecting the most radiation is then given as:

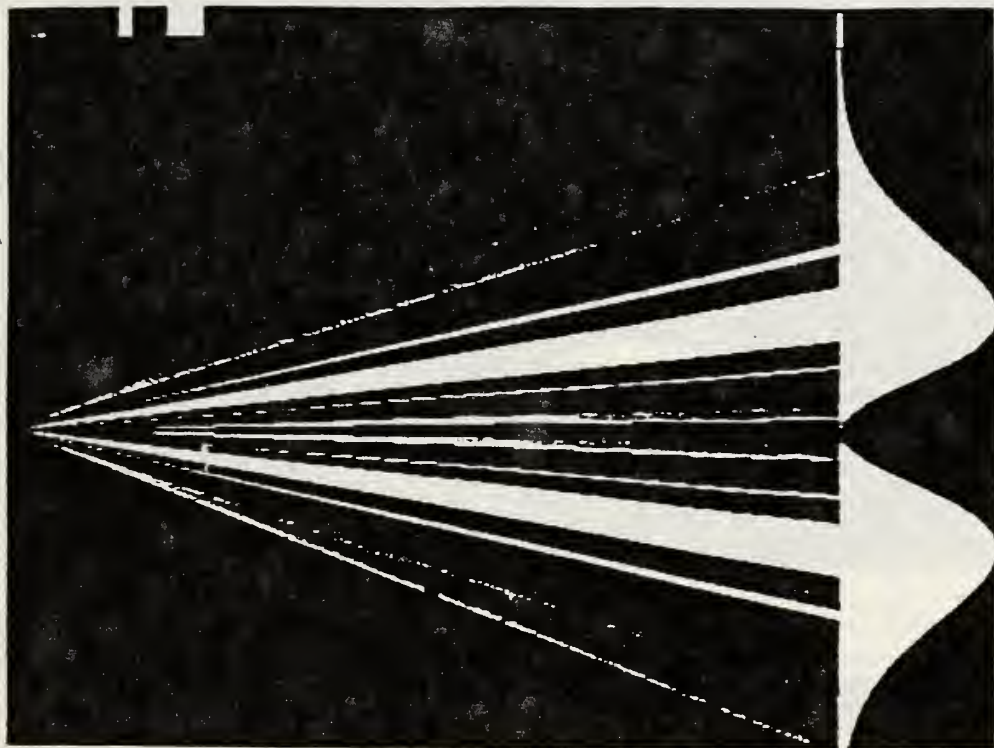
$$\theta_{opt}^2 = 1/5(\delta_1 + \delta_2) + [(\delta_1 + \delta_2)^2 - 60\delta_1\delta_2]^{1/2} \quad (2.3)$$

where

$$\delta_i = \frac{1}{2\gamma^2} + \frac{\omega_i^2}{2\omega^2} \quad (2.4)$$

Using the geometry shown in Figure 5, along with  $\theta_{opt}$  as calculated above, and given a finite electron beam diameter  $d_1$  and finite focal spot diameter  $d_2$ ; the optimum diameter, length, and placement of the cylindrical optic can be determined. As can be seen from Figure 5:

$$D = L_3 \tan \theta_{opt} \quad (2.5)$$



Emission  
Profile

Figure 2. Computer ray tracing simulation and emission profile of the x-rays generated from a transition radiator without focusing optics. The vertical dimension is greatly magnified relative to the horizontal.

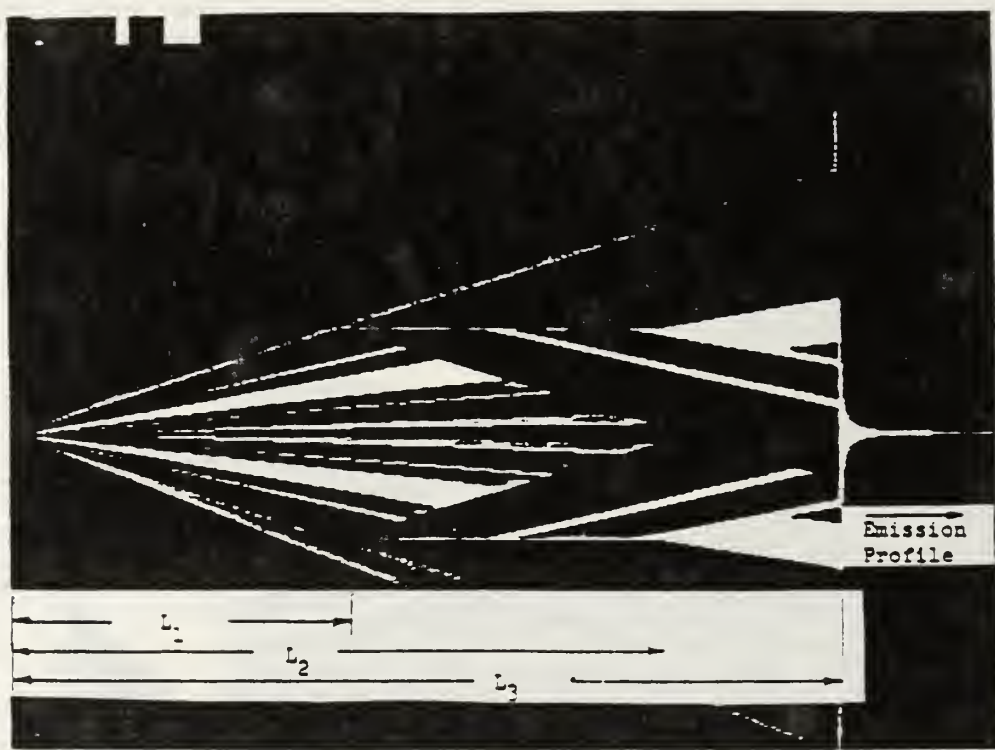


Figure 3. Computer ray tracing simulation and emission profile of the x-rays generated from a transition radiator with focusing optics. The vertical dimension is greatly magnified relative to the horizontal.

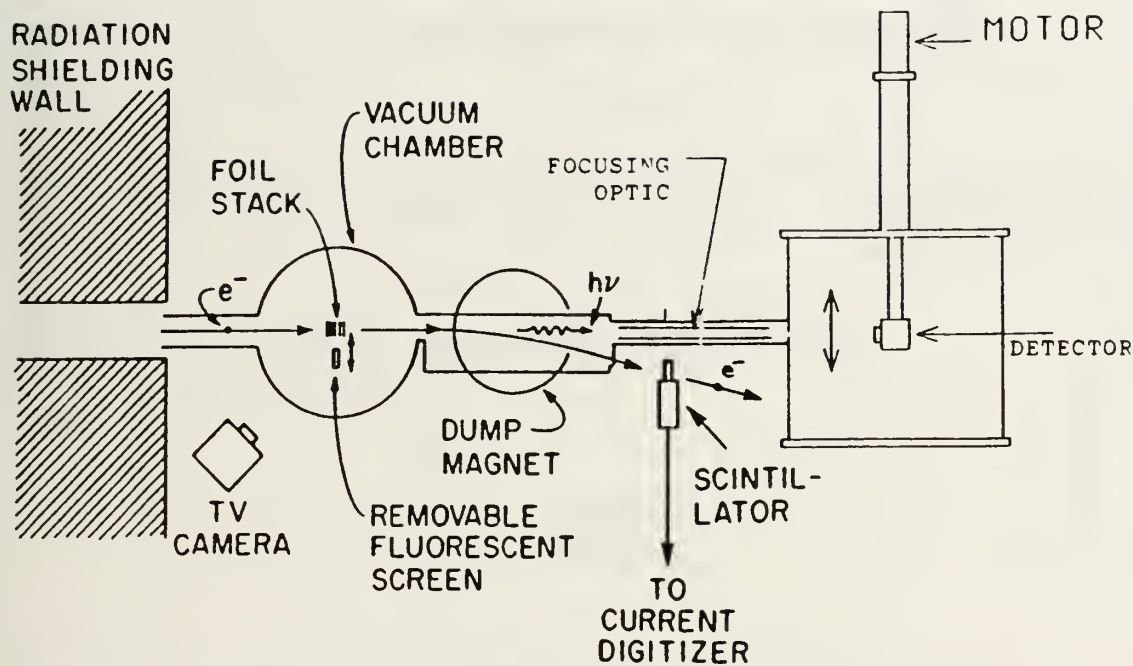


Figure 4. Monterey NPS experiment. The electron beam enters from the left where it strikes the foil stack and x-rays are emitted downstream. The dump magnet separates the electrons from the x-rays. The focusing optic reflects the x-rays to a focus at the detector.

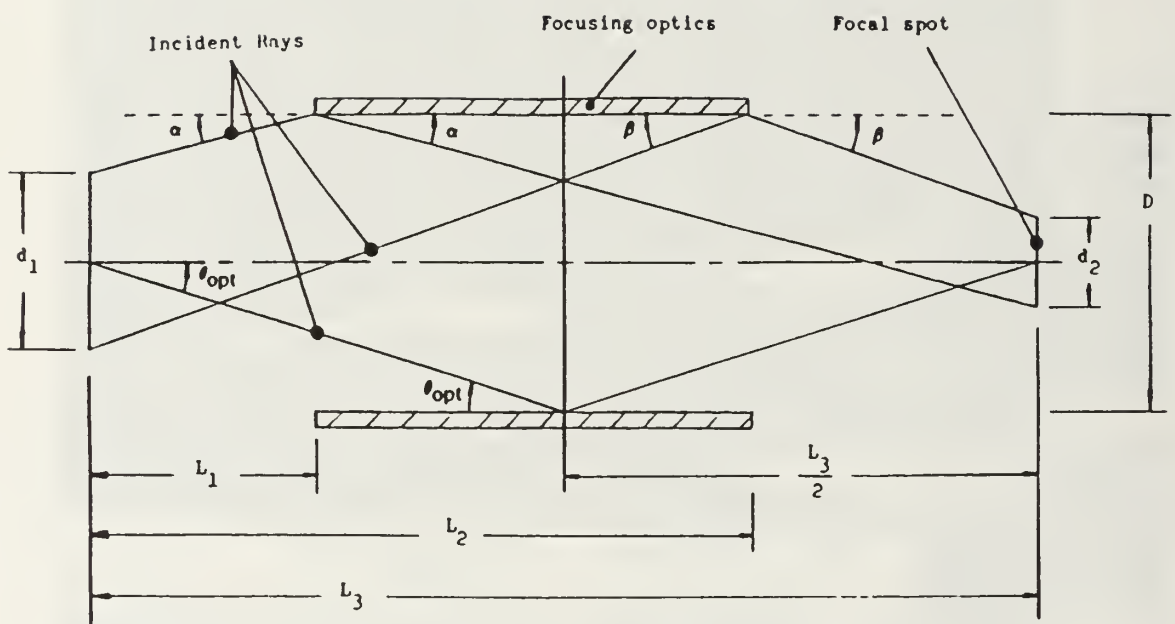


Figure 5. A cross sectional view of the hollow cylindrical optic focusing system showing the conditions for focusing a finite diameter beam. The tube diameter  $D$ , the beam diameter  $d_1$ , the focal spot diameter  $d_2$ , the lengths  $L_1$ ,  $L_2$ ,  $L_3$ , and the angles  $\alpha$ ,  $\beta$ , and  $\theta_{opt}$  are shown.

Calculating the dimensions necessary to reflect extreme rays to the point of focus we see that:

$$\tan \alpha = \frac{D-d_1}{2L_1} = \frac{D+d_2}{2(L_3-L_1)} \quad (2.6)$$

therefore:

$$L_1 = \frac{L_3(D-D_1)}{2D+d_2-d_1} \quad (2.7)$$

and:

$$\tan \beta = \frac{D+d_1}{2L_2} = \frac{D-d_2}{2(L_3-L_2)} \quad (2.8)$$

where  $\beta$  is the angle defined in Figure 5.

therefore:

$$L_2 = \frac{L_3(D+d_1)}{2D+d_1-d_2} \quad (2.9)$$

Therefore, given the diameter of the electron beam  $d_1$ , the diameter of the focal spot  $d_2$ , and the location of the detector plane  $L_3$ ; the tube length  $L=L_2-L_1$  and its position  $L_1$  and  $L_2$  can be determined.

In summary, the procedure for designing the cylindrical optics is as follows:

- 1) Calculate  $\theta_{opt}$  from equation 2.3. Parameters needed include: electron beam energy, plasma frequency of the foil material and spacing medium, and the angular frequency of maximum photon emission.
- 2) Calculate the diameter of the optic using equation 2.5. Parameters needed are  $\theta_{opt}$  and the distance to the desired focal point.
- 3) Calculate the locations of the optics entrance and exit using equations 2.7 and 2.9, respectively. Parameters needed include: the distance to the desired focal point, diameter of the electron beam, diameter of desired focal spot, and the diameter of the optic.

#### C. CYLINDRICAL FOCUSING SIMULATION

For a given electron beam of energy E incident upon a stack of M foils of thickness  $l_1$ , separation  $l_2$ , plasma frequency  $\omega_p$ , and energy dependent absorption coefficient, the flux (photons/electrons/sr) as a function of angle is calculated. A typical example is shown in Figure 6. Using this as an input, along with the specified dimensions and placement of the cylindrical optic, the x-ray intensity profile produced by a TR source coupled to the optic is predicted. A typical example is shown in Figure 7. Figure 8 shows a direct comparison of TR before and after focusing from a previous experiment [Ref. 6].

#### D. ENERGY AND ANGULAR DEPENDENT REFLECTIVE LOSSES

There are three ways that the intensity of an x-ray reflecting from a material surface can be attenuated:

MYLAR, 93MeV, 8 FOILS.

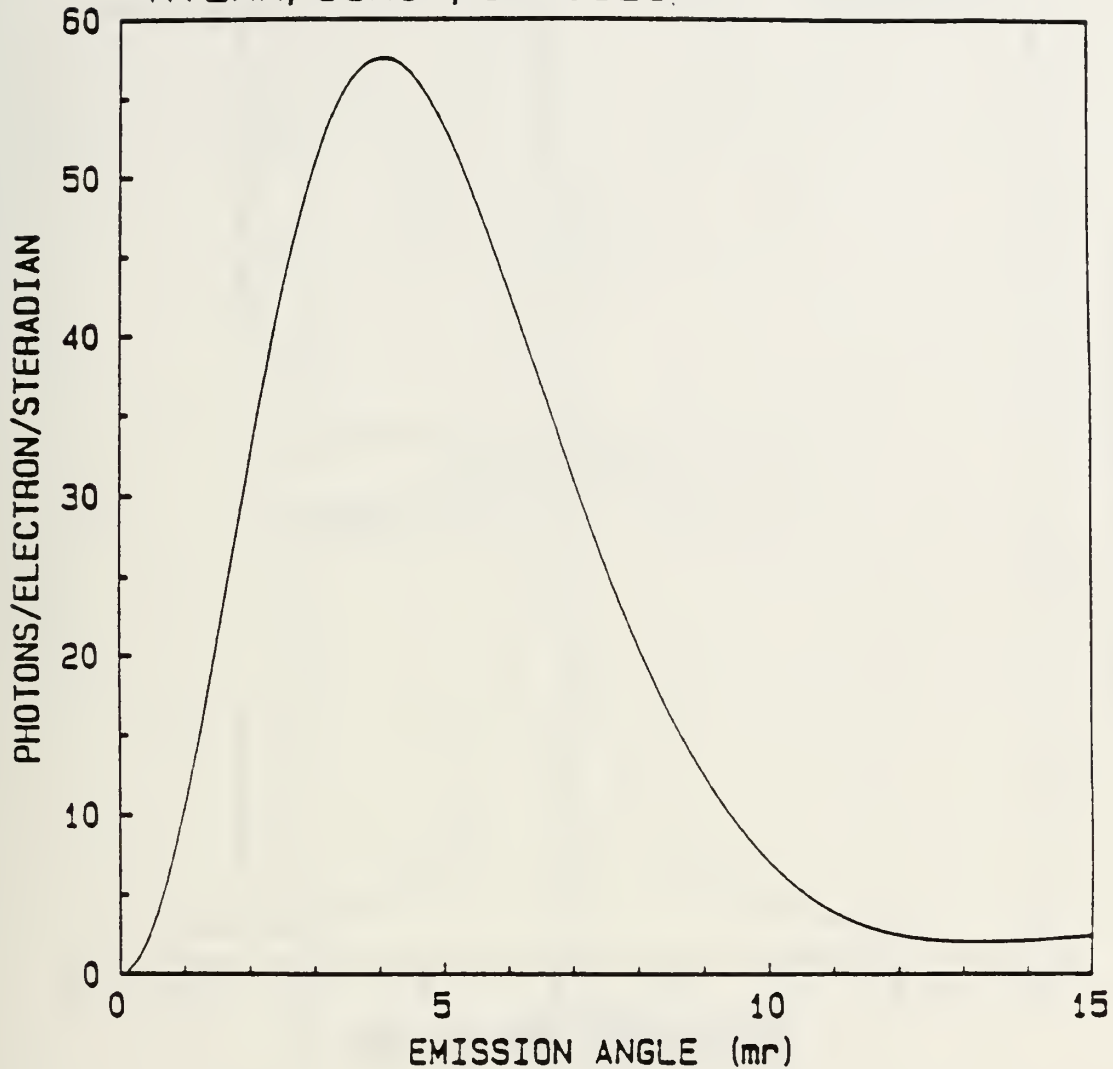


Figure 6. The calculated emission profile of soft x-rays generated from a transition radiator without focusing optics.

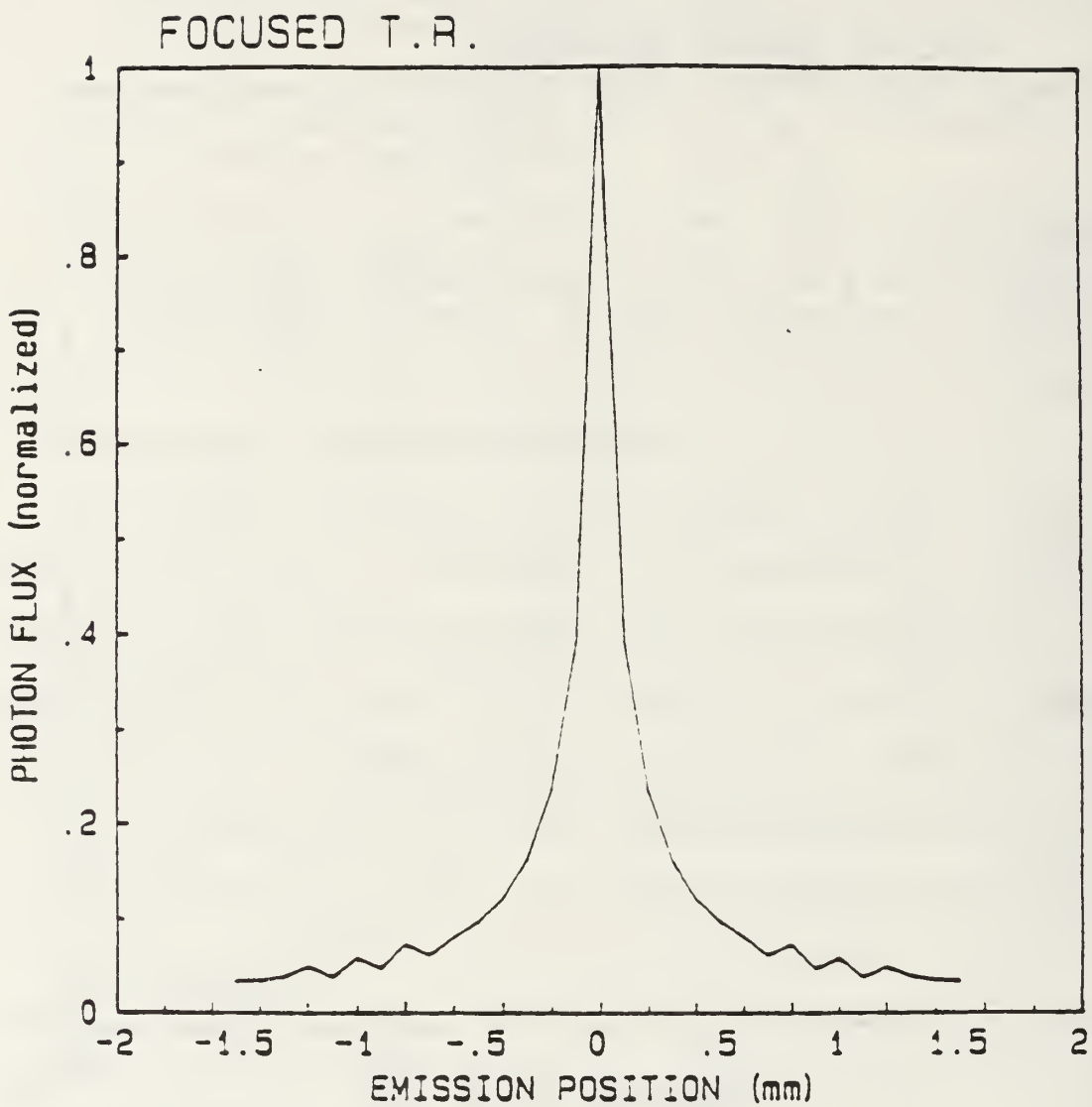


Figure 7. The calculated emission profile of soft x-rays generated from a transition radiator with focusing optics.

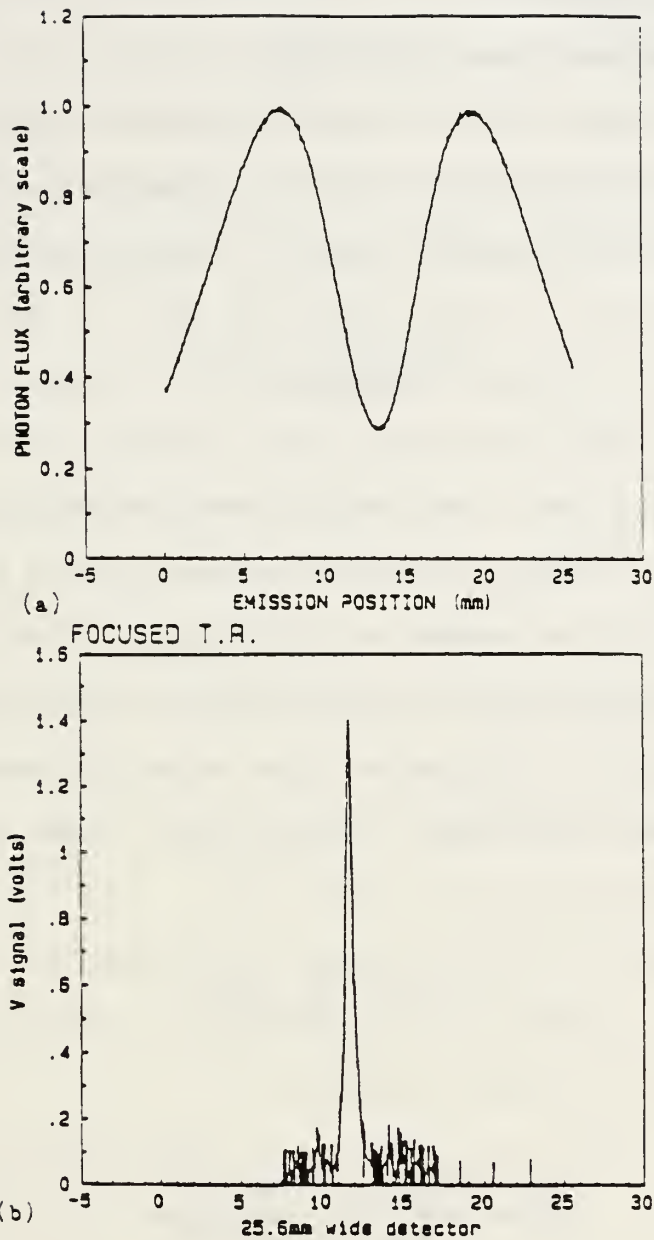


Figure 8. A measured profile of soft x-rays generated by a 93 MeV electron beam incident upon a stack of eight 3.5  $\mu\text{m}$ -thick foils. The profile was measured at a distance  $L_3=1.35$  m from the foil stack.

- (a) without cylindrical optic
- (b) with cylindrical optic

- 1) Transmission Loss
- 2) Absorption
- 3) Surface Roughness Deflection

When an x-ray beam strikes a solid surface, a portion of the beam is reflected and a portion is transmitted. The portion that is transmitted depends mainly on the real part of the dielectric constant of the material and on the angle of incidence of the incoming x-ray beam. The larger the angle of incidence, the larger the transmitted portion of the beam will be. Absorption of the x-ray beam depends primarily on  $\beta$ , the imaginary part of the dielectric constant given in equation 2.1. Absorption of the beam is that portion that is neither reflected nor transmitted. Lastly, when the surface of the reflecting material is uneven, the incoming beam will be deflected in many different directions. The rougher the surface, the larger this loss will be.

The amplitude of the reflected x-ray beam can be found in classical electro-dynamic theory [Ref. 9], which accounts for the transmission loss and absorption:

$$\frac{R_t}{A_t} = \frac{n^2 \sin \theta_i - (n^2 - \cos^2 \theta_i)^{1/2}}{n^2 \sin \theta_i + (n^2 - \cos^2 \theta_i)^{1/2}} \quad (2.10)$$

$$\frac{R_n}{A_n} = \frac{\sin \theta_i - (n^2 - \cos^2 \theta_i)^{1/2}}{\sin \theta_i + (n^2 - \cos^2 \theta_i)^{1/2}} \quad (2.11)$$

where the index of refraction,  $n$ , is a complex number and  $\theta_i$  is the angle of incidence.  $A_t$  and  $A_n$  are the magnitudes of the tangential and normal components of the incident electric field and  $R_t$  and  $R_n$  are the corresponding magnitudes of the reflected electric field. Therefore the reflectivity is given by:

$$R_p = \left( \frac{Rn^2 + Rt^2}{An^2 + At^2} \right)^{1/2} \quad (2.12)$$

In this experiment we have a plane wave travelling in a vacuum incident on a smooth planar boundary of quartz or nickel with a complex index of refraction as given in equation 2.1 with the imaginary part,  $\beta$ , being negligible compared to the real part in the soft x-ray energy range [Ref. 10]. If  $\theta_i$  has the value of  $\theta_c$  given by equation 2.2, then equations 2.10, 2.11, and 2.12 reduce to:

$$\frac{Rt}{At} = \frac{Rn}{An} = R_p = 1$$

i.e., the incident wave is totally reflected. If  $\theta_i$  is less than  $\theta_c$ , again, no radiation can propagate in the optic and the wave is totally reflected.

Using the effect of a displaced lattice on x-ray scattering as a model for surface roughness deflection, the attenuation of the intensity is given by [Ref. 9]:

$$\frac{I_d}{I_i} = \exp\left[-\left(\frac{4\pi\sigma\sin\theta_i}{\lambda}\right)^2\right] \quad (2.13)$$

where  $\sigma$  is the rms roughness of the surface,  $\lambda$  is the x-ray wavelength,  $I_d$  and  $I_i$  are the attenuated and ideal intensities. Since the first Fresnel zone is much larger than the mean period of the roughness  $\bar{s}$ , i.e.:

$$\bar{s} < \frac{(\pi\sigma\lambda)^{1/2}}{\sin\theta_i} \quad (2.14)$$

This model is valid, and this condition is certainly satisfied by TR where, as previously shown,  $\theta_i$  is on the order of mrad (e.g.,  $\theta_i=10$  mrad given an electron beam of 50 MeV). Therefore the total reflectivity is given by the product of  $R_p$  and  $I_d/I_i$  as given by equations 2.12 and 2.13 respectively. Furthermore, if  $\theta_i$  is less than  $\theta_c$ ,  $R_p=1$  and the total reflectivity is given solely by equation 2.13.

Examining these formulas shows a dependence on the angle and frequency of the beam. Given a 93 MeV electron beam incident on a stack of 8 mylar foils, 3.5  $\mu\text{m}$  thick, and assuming 2 keV x-rays are produced, the influence of optics loss [Ref. 6] on the flux intensity profile is shown in Figure 9. Results are shown for the case of no loss, the case of loss with zero surface roughness, and the case of loss with 25

nm rms surface roughness. The calculation assumes that  $\beta$  is negligible and  $n = .999559$ . Figure 10 [Ref. 6] shows a plot of the energy and angular dependant reflective loss coefficient for a 1 nm rms surface roughness given the same parameters.

#### E. ELLIPTICAL OPTICS

The main objective of this experiment was to focus as much of the TR cone as possible. In order to achieve this objective a straight-walled surface with a circular cross section will not suffice. However, elliptical optics can provide the required geometry that will focus the entire radiation cone to a single point. Using elliptical optics has the possibility of increasing the overall intensity of the focal spot by one to two orders of magnitude in comparison to straight walled optics [Ref. 6].

A mathematical property of an ellipse states that if a ray is emitted at one focal point it will be reflected and ultimately travel through the other focal point [Ref. 11]. As is the case with straight-walled optics, this will occur only if the angle of incidence is less than the critical angle, as given by equation 2.2. The only requirement is that the surface of revolution around the major axis of the ellipse be made to reflect the entire radiation cone.

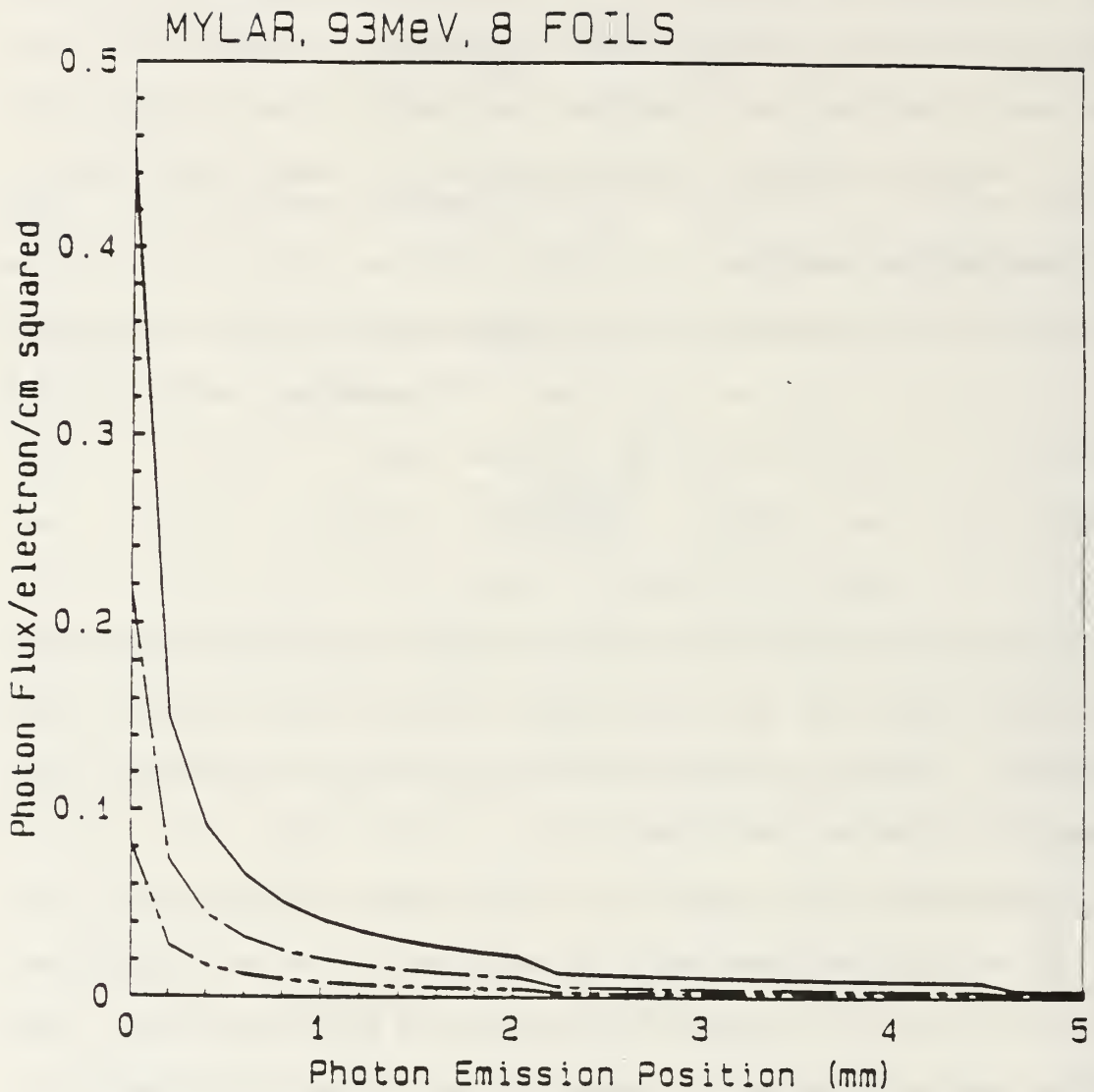


Figure 9. The calculated emission profile of soft x-rays generated from a transition radiator with focusing optics. The calculation shows the influence of the angular and energy dependent reflective loss on the peak amplitude of the focused radiation. Solid curve: calculated for idealized lossless optics. Once dash curve: calculated for real optics with 1 nm RMS roughness. Two dash curve: calculated for real optics with 25 nm RMS roughness.

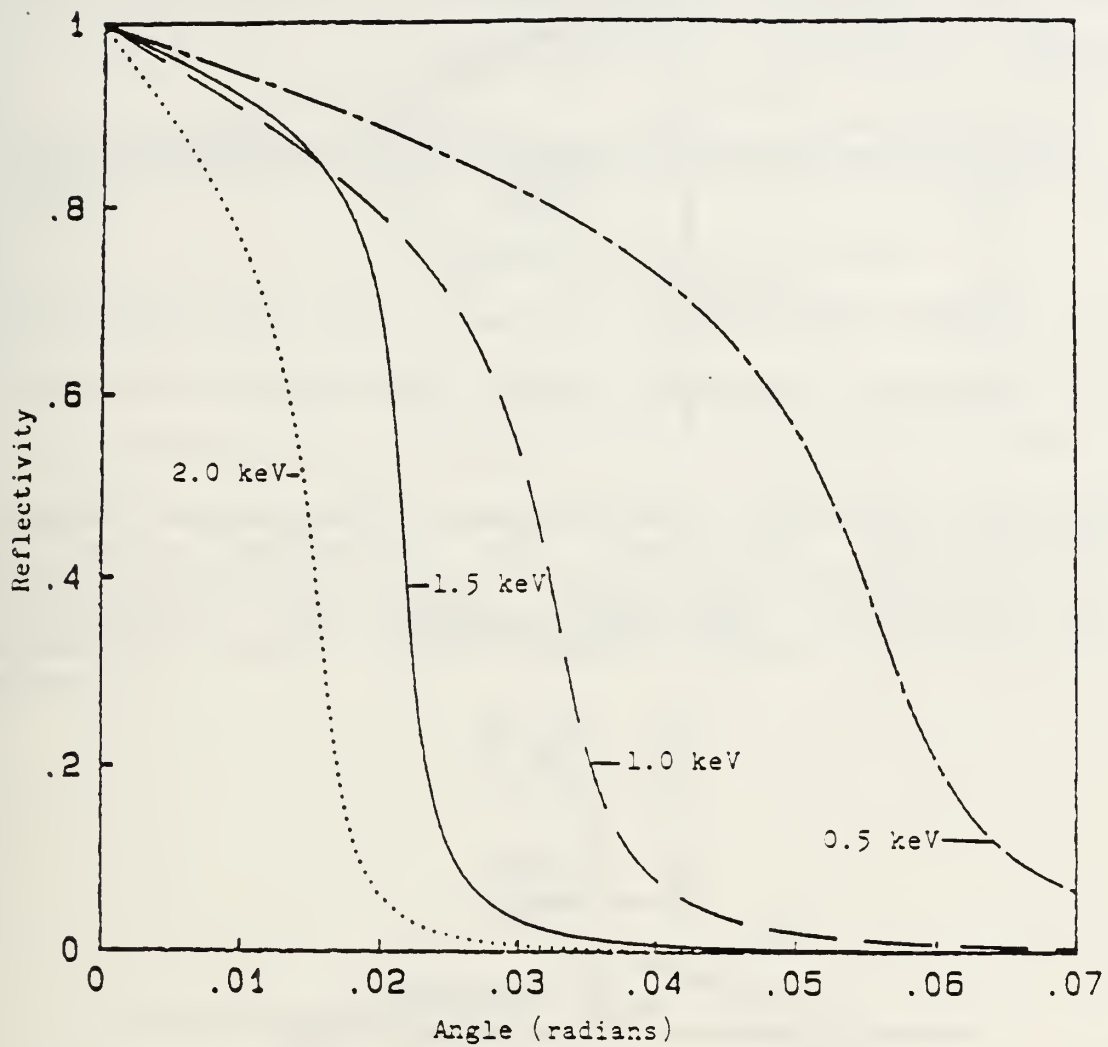


Figure 10. The calculated reflectivity of quartz as a function of angle and x-ray energy.

Given the parameters of the TR cone, the dimensions of the ellipse can be calculated from the polar equation of an ellipse:

$$r = \frac{a(1-e^2)}{1+e\cos\theta} \quad (2.15)$$

where  $a$  is the radius of the major axis,  $e$  is the eccentricity of the ellipse,  $x=rcos\theta$ , and  $y=rsin\theta$ . See Figures 11 and 12. The needed eccentricity of the ellipse is calculated [Ref. 9] by obtaining the slope of the tangent to the ellipse,  $dy/dx$ .

$$\frac{dy}{dx} = \sin\theta \frac{dr}{dx} + r\cos\theta \frac{d\theta}{dx} \quad (2.16)$$

$$\frac{dr}{dx} = \left(\frac{dr}{d\theta}\right) \left(\frac{d\theta}{dx}\right)$$

$$\frac{dr}{d\theta} = \frac{resin\theta}{1+e\cos\theta}$$

$$\frac{dx}{d\theta} = -r\sin\theta + \frac{resin\theta\cos\theta}{1+e\cos\theta}$$

$$\frac{d\theta}{dx} = \left(\frac{1+e\cos\theta}{r\sin\theta}\right)$$

substituting

$$\frac{dy}{dx} = \left(\frac{resin^2\theta}{1+e\cos\theta} + r\cos\theta\right) \left(\frac{-1-e\cos\theta}{r\sin\theta}\right) \quad (2.17)$$

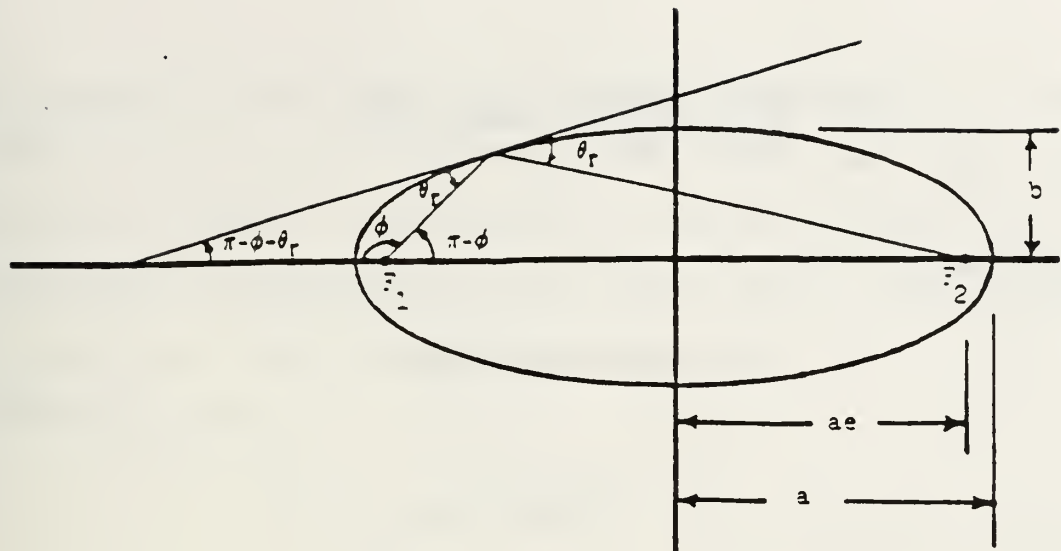


Figure 11. A schematic cross-sectional view of the elliptical wall hollow cylindrical optic showing the conditions for focusing the divergent cone of transition radiation originating at point  $F_1$  and focused at point  $F_2$ . The semimajor axis  $a$ , semiminor axis  $b$ , and distance from center for focus are shown.

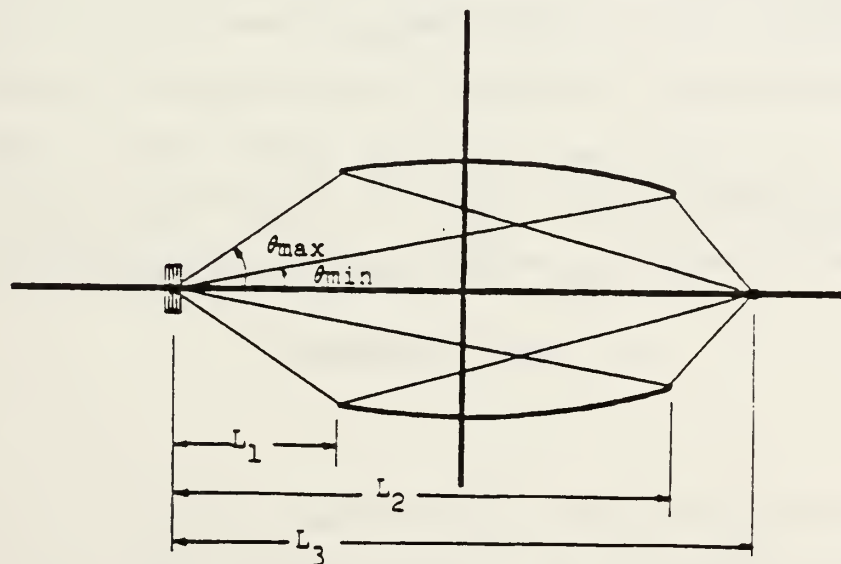


Figure 12. A schematic of the use of a finite dimensional elliptical optic to focus the transition radiation cone produced by a foil stack.

$$\frac{dy}{dx} = \frac{-\cos \theta - e}{\sin \theta} = \tan(\pi - \theta - \theta_c) \quad (2.18)$$

solving for  $e$ ,

$$e = -\tan(\theta - \theta_c) \sin \theta + \cos \theta \quad (2.19)$$

where  $\theta$  is defined as  $\pi - \phi$ . Since  $\theta_c < \theta < \theta_c$ , let:

$$\theta = \theta_c - \epsilon_1 \quad (2.20)$$

and

$$\theta_c = \theta - \epsilon_2 \quad (2.21)$$

Subtracting equation 2.21 from 2.20, given that  $\epsilon_1$  is the same order of magnitude as  $\epsilon_2$ , equation 2.19 can be written as:

$$e = -\tan(\theta_c - \theta) \sin \theta + \cos \theta \quad (2.22)$$

The maximum TR cone angle is approximately  $\frac{3}{2\gamma}$  and the minimum angle is approximately  $\frac{1}{2\gamma}$ . Substituting these limits into equation 2.22,

$$e = -\tan(\theta_c - \frac{1}{2\gamma}) \sin(\frac{1}{2\gamma}) + \cos(\frac{1}{2\gamma}) \quad (2.23)$$

For example, if  $E=50$  MeV, the plasma frequency  $\omega_p=33.2$  eV, and the x-ray photons have an energy of 2 keV; then  $\frac{1}{2\gamma}=5$ mrad and  $\theta_c=16.61$  mrad. Using equation 2.23, the eccentricity of the ellipse is calculated to be 0.99992. Then, given a value for the major axis  $a$ , the required minor axis  $b$  can be calculated from:

$$b = a\sqrt{1-e^2} \quad (2.24)$$

Table I shows design parameters for 25, 50, and 100 MeV beam energies. It is assumed that the peak emission is produced at an angle of  $\frac{1}{\gamma}$  and that the emission ranges from  $\frac{1}{2\gamma}$  to  $\frac{3}{2\gamma}$ . The critical angle has been calculated using equation 2.2. The distance from the source at one foci of the ellipse to the focal spot at the other foci of the ellipse is  $L_3$ , and therefore the major axis  $a$  is  $L_3/2$ . The calculations were made for two different values of  $L_3$  [Ref. 6].

TABLE I. DESIGN PARAMETERS FOR AN ELLIPTICAL OPTIC GIVEN VARIOUS ELECTRON BEAM ENERGIES. THE PARAMETERS WERE DEFINED IN THE PREVIOUS SECTIONS.

BEAM ENERGY	25 MeV	50 MeV	100 MeV
$1/2\gamma(\text{mr})$	10.24	5.12	2.56
$1/\gamma(\text{mr})$	20.48	10.24	5.12
$3/2\gamma(\text{mr})$	30.72	15.36	7.68
$e_{\min}$	0.99988	0.99992	0.99996
Given: $L_3 = 1.35 \text{ m}$			
DIAMETER @ $L_1(\text{mm})$	16.6	15.7	11.8
DIAMETER @ $L_2(\text{mm})$	19.3	11.7	6.4
DIVERGENCE @ FOCUS (mr)	23	28	31
a (mm)	675.08	675.05	675.03
b (mm)	10.36	8.10	5.98
$L_1(\text{m})$	0.27	0.51	0.77
$L_2(\text{m})$	0.94	1.14	1.25
Given: $L_3 = 3 \text{ m}$			
a (mm)	1500.34	1500.21	1500.12
b (mm)	32	25	19
$L_1(\text{m})$	1	1.1	1.2
$L_2(\text{m})$	2	1.9	1.8

### III. EXPERIMENTAL SETUP AND PROCEDURE

The experimental setup is shown in Figure 4. It consisted of the linear accelerator (linac), main scattering chamber, dump magnet, focusing optic, and x-ray detector.

#### A. LINAC

The linac is a three section, pulsed, S-band RF accelerator with an energy from 20-100 MeV and average currents of less than 0.25 microampere. The beam pulse duration is about one microsecond and the pulse repetition rate is 60 Hz. Electrons, generated by an electron gun, are accelerated by riding an RF wave through three stages of acceleration. Once accelerated, the electron beam is deflected by magnets into the main scattering chamber as shown in Figure 13. The control room has the control equipment for the acceleration of the electrons and to steer the beam into the target areas.

#### B. MAIN SCATTERING CHAMBER

The main scattering chamber is a 24 inch diameter vacuum chamber. At the center of the chamber there is a target ladder which can be raised, lowered, and rotated. Several viewing ports provide for visual and video alignment of the target. The target ladder controls are located at the linac operation panel, and stepping motors remotely control the

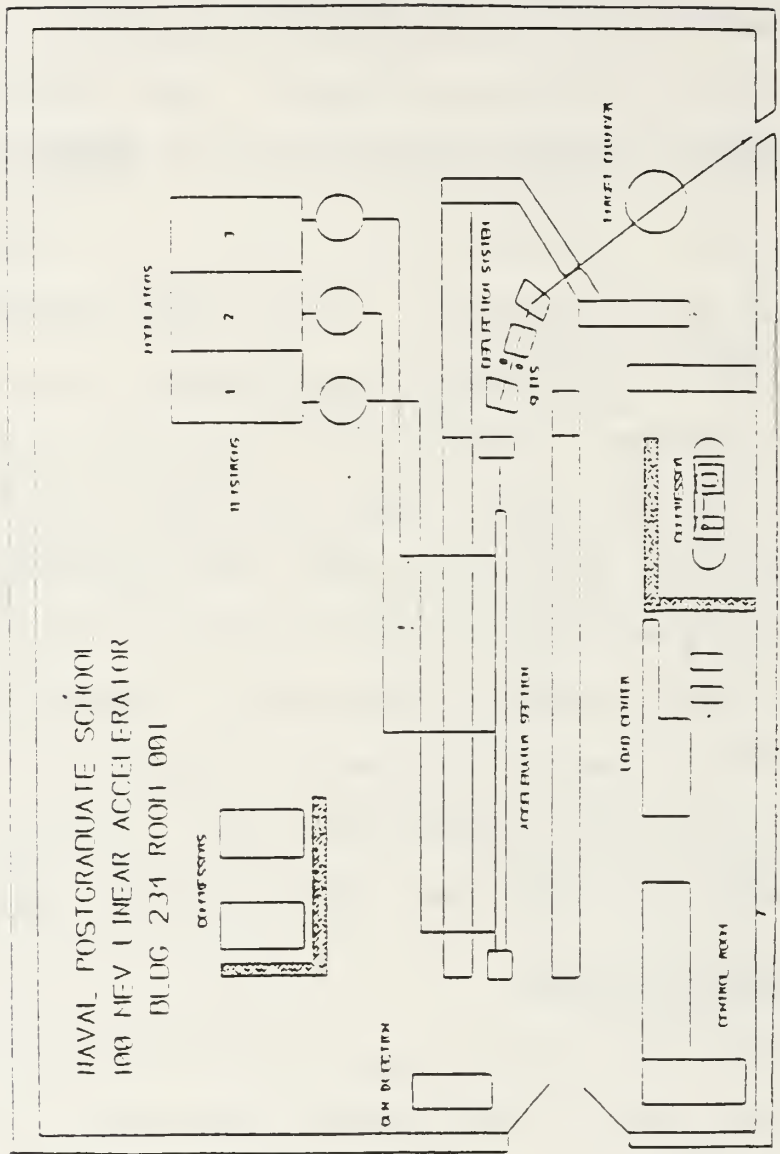


Figure 13. Linear Accelerator equipment layout.

vertical position and rotation of the ladder in the main scattering chamber.

#### C. DUMP MAGNET

Once the electron beam transverses the foil stack (target) in the main scattering chamber, and the diverging cone of TR is produced, the electron beam must be diverted. This is accomplished by placing a deflection magnet in the path of the beamline.

#### D. FOCUSING OPTICS

Both a cylindrical quartz optic and a nickel plated elliptical optic were used in this experiment. The nickel optic was manufactured by Adelphi Tech. Inc., and the quartz optic was a standard glass tube that may be purchased by one of many vendors. The optics specifications are listed in Table II.

#### E. LINEAR IMAGE SENSOR

A 25.6 mm long linear diode array, manufactured by Hamamatsu Corp., was used for detecting the soft x-ray intensity profile. This array consists of 512 silicon diodes on 50 micron centers. It allowed real time observation of a one-dimensional image of the spatial distribution at focus. The detector is sensitive to photons in the energy range of 1-

10 keV, and therefore well suited for soft x-rays. Each detector element has a photosensitive area 50 micron wide by 2.5 mm high. As an option, slits can be placed in front of the detector to reduce the effective height, thus providing better resolution. The incident photons produce a charge which is accumulated on the individual detector element capacitors, and the voltage across each capacitor is read out serially during an analog readout cycle. The analog voltage signal from the diode array was input to a Metrabyte 12-bit Analog to Digital Converter, and the subsequent intensity profile was displayed on an IBM AT computer. This image was also displayed on an oscilloscope on a pulse to pulse basis, and the electron beam parameters were varied to achieve maximum peak photon flux at focus.

#### F. ALIGNMENT

The foil stacks were placed in the geometric center of the main scattering chamber perpendicular to the incoming electron beam. The optics were mounted with the tube entrance 1.4 meters and the tube exit 1.7 meters from where TR exits the foil stack. The optics were located concentric to the inside of a 1.5 inch diameter vacuum pipe downstream of the dump magnet. The linear image sensor was placed at a distance of 3.0 meters from the foil stack exit. The electron beam was

passed through the foil stack, TR was produced, focused by the optics, and collected by the linear image sensor.

TABLE II. CHARACTERISTICS OF X-RAY IMAGINING OPTICS USED

	Quartz	Nickel
Length (cm)	30.5	30.5
Diameter @ L (mm)	10	10
Diameter @ L (mm)	10	10
Semi-Major Axis (mm)	N/A	1500
Semi-Minor Axis (mm)	N/A	12.7
Eccentricity	N/A	.99996
Surface Roughness* (nm)	7.0	14

\* The surface roughness of the quartz cylindrical optic was determined by a contact measurement using a Dectack, whereas the surface roughness of the nickel elliptical optic was determined by a non-contact measurement using an inferometer [Ref. 12].

#### IV. RESULTS

The above procedure was repeated several times, varying the following parameters:

- 1) Type of Optic
- 2) Electron Beam Energy
- 3) Type of Foil Stack
- 4) Inclusion of Slits

These parameters are summarized in Table III. It should be noted that trials 9 and 10 included covering the optic entrance with 6.5 microns of mylar. This was an attempt to filter the low energy x-rays and will be explained in more detail in the next chapter.

In order to produce intensity profiles, several conversions to the computer generated data had to be made. The capacitance,  $C$ , of the Hamamatsu detector is 4.5 pF [Ref. 13]. The detector conversion efficiency,  $v_1$ , between 1-5 keV is approximately 0.22 Coulombs per joule [Ref. 14]. The area of the detector,  $A$ , with and without slits is  $0.02 \text{ mm}^2$  and  $0.125 \text{ mm}^2$  respectively [Ref. 13]. The numbers generated by the computer,  $N$ , are voltage times four [Ref. 13]. The pulse duration,  $t_s$ , is 16.7 msec. The current,  $I_s$ , is displayed on the secondary emission monitor which has an efficiency,  $v_2$ , of 0.127 [Ref. 15]. Taking all of these factors into account the final conversion becomes:

$$\frac{PhotonFlux}{(J/coulomb/mm^2)} = \frac{CNv_2}{4v_1AI_s t_d}$$

This conversion was made to the computer generated data and the one-dimensional intensity profiles corresponding to Table III were produced. The profiles are shown in Figures 14-23. The diameter of the focal spot is represented by the FWHM.

TABLE III. PARAMETERS OF INDIVIDUAL X-RAY FOCUSING EXPERIMENTS

Trial #	Optic	Energy (MeV)	Current (amps)	Foil Stack	Slits
1	Nickel	89	$2.76 \times 10^{-7}$	Al	No
2	Nickel	85	$5.91 \times 10^{-8}$	Al	No
3	Nickel	61	$1.97 \times 10^{-7}$	Al	No
4	Quartz	92	$4.72 \times 10^{-7}$	Al	No
5	Quartz	65	$1.18 \times 10^{-7}$	Al	No
6	None	89	$3.15 \times 10^{-7}$	Al	No
7	Nickel	96	$3.94 \times 10^{-7}$	Ti	Yes
8	Quartz	95	$1.26 \times 10^{-7}$	Ti	Yes
9	Nickel	95	$4.72 \times 10^{-7}$	Ti	Yes
10	Quartz	95	$2.36 \times 10^{-7}$	Ti	Yes

Note 1: The current is based on an S.E.M. efficiency of 0.127.

Note 2: Trials 9 and 10 were taken with 6.5 microns of mylar covering the entrance of the optics.

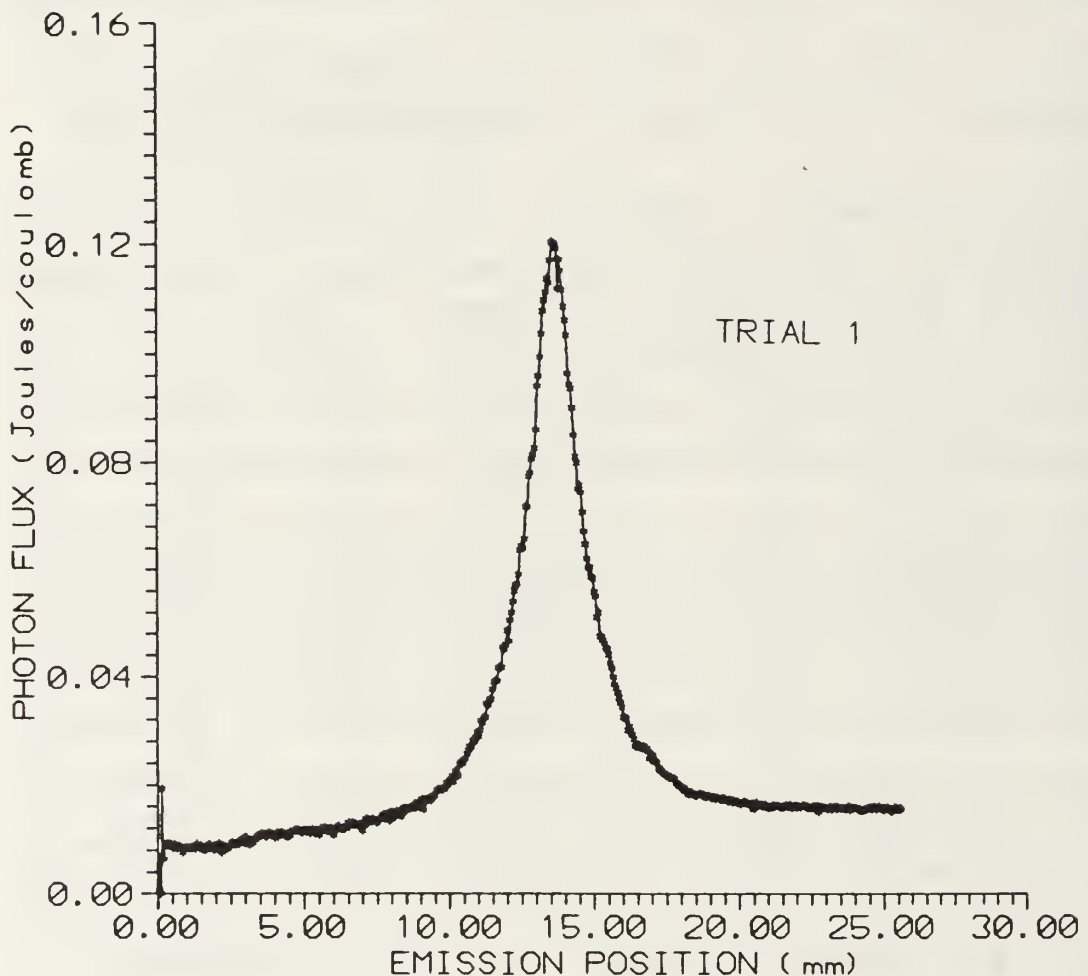


Figure 14. Measured 1-D emission profile of soft x-rays focused by a nickel elliptical optic. The soft x-rays were produced by an 85 MeV electron beam incident on a 10 foil stack of aluminum with 1  $\mu\text{m}$  thick foils. The flux at peak height is 0.12 J/coulomb and the FWHM is 2.45 mm.

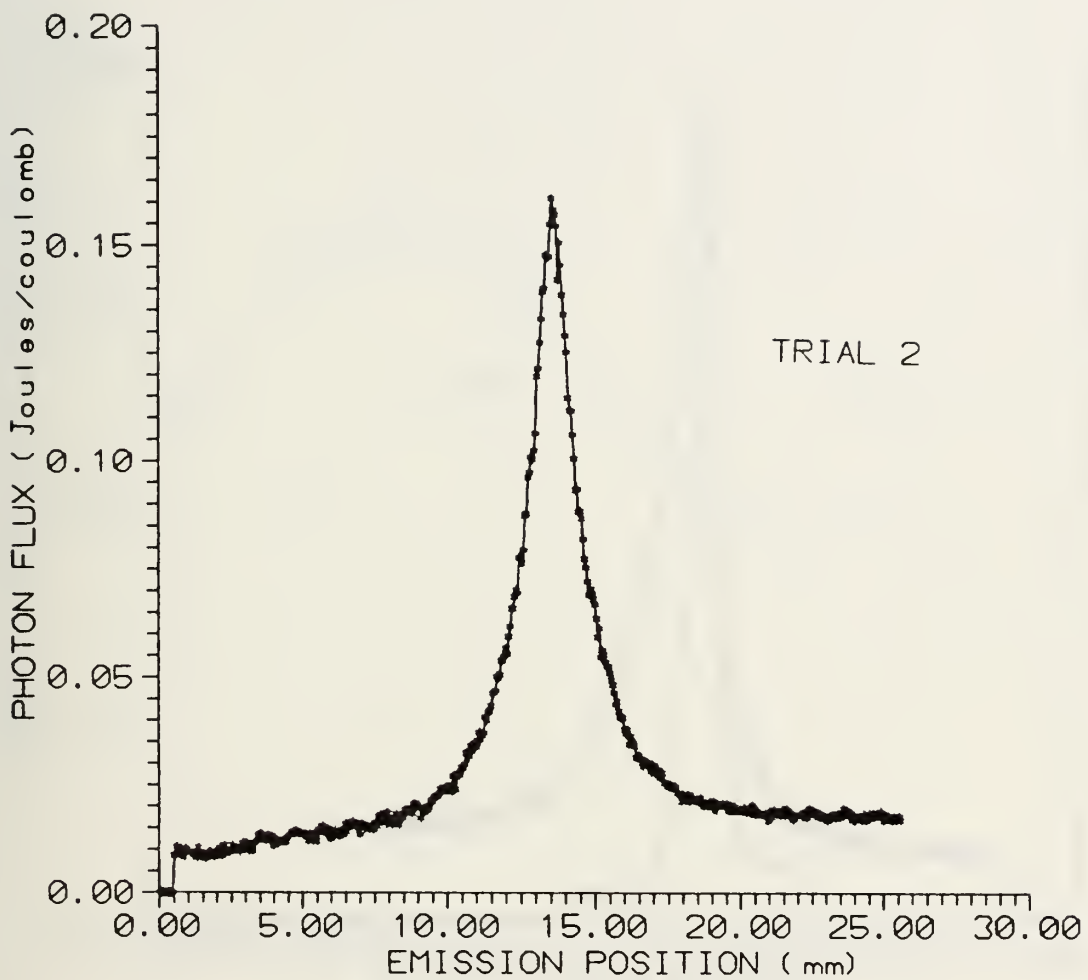


Figure 15. Measured 1-D emission profile of soft x-rays focused by a nickel elliptical optic. The soft x-rays were produced by an 85 MeV electron beam incident on a 10 foil stack of aluminum with 1  $\mu$ m thick foils. The flux at peak height is 0.16 J/coulomb and the FWHM is 2.00 mm.

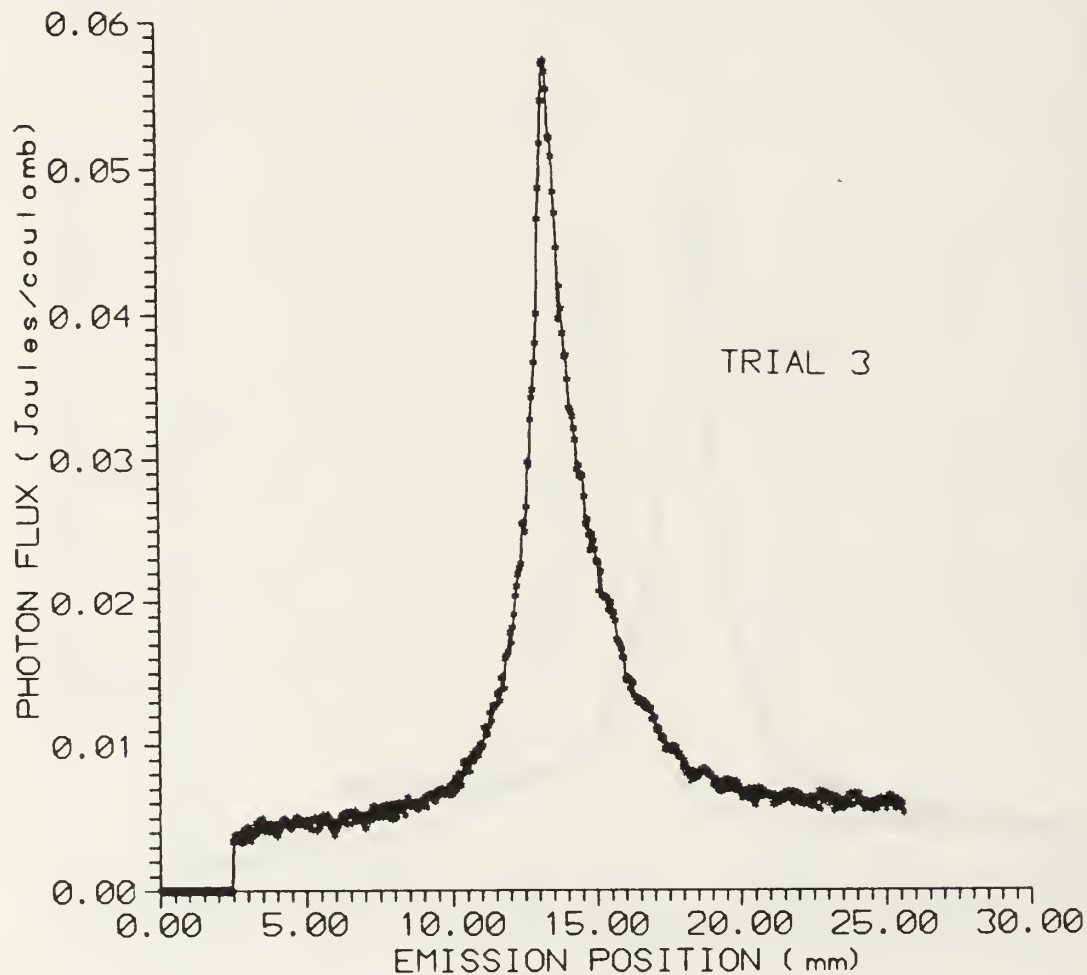


Figure 16. Measured 1-D emission profile of soft x-rays focused by a nickel elliptical optic. The soft x-rays were produced by a 61 MeV electron beam incident on a 10 foil stack of aluminum with 1  $\mu\text{m}$  thick foils. The flux at peak height is .058 J/coulomb and the FWHM is 1.82 mm.

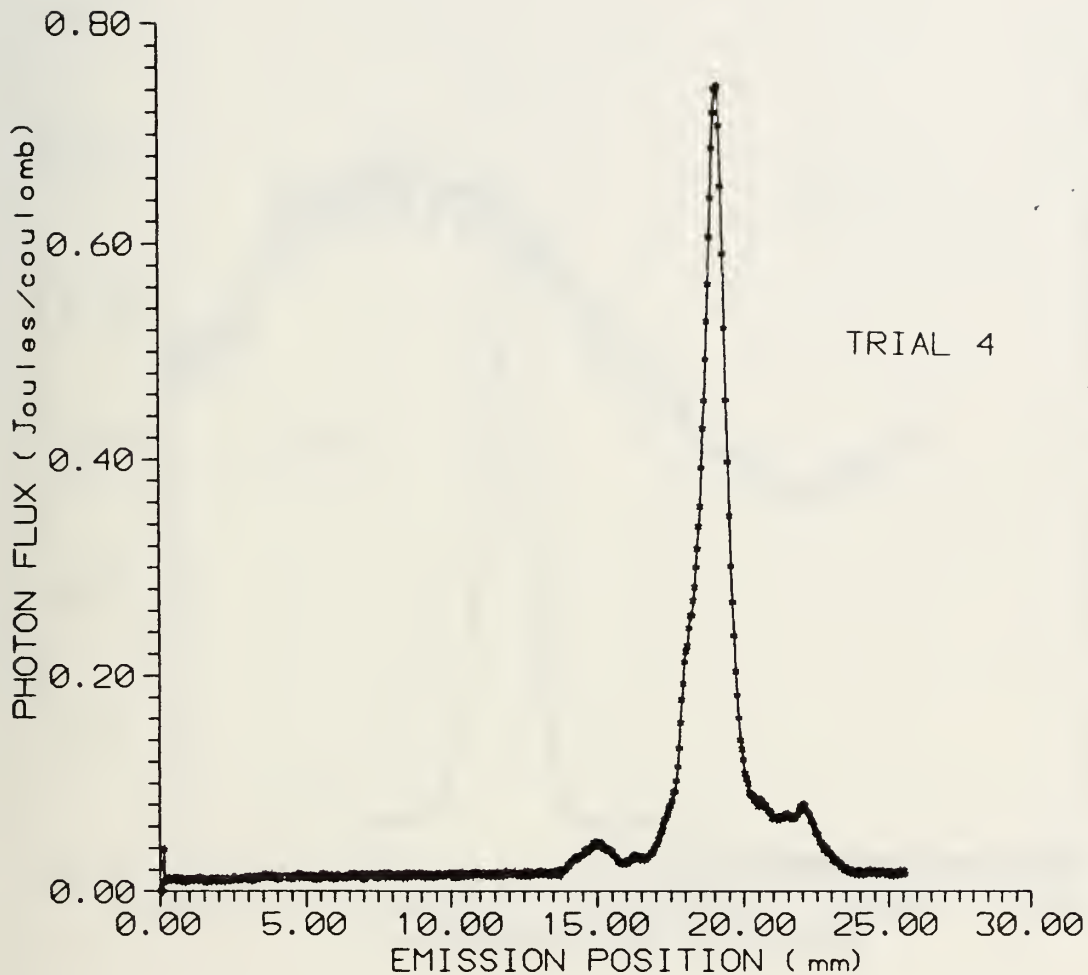


Figure 17. Measured 1-D emission profile of soft x-rays focused by a quartz elliptical optic. The soft x-rays were produced by a 92 MeV electron beam incident on a 10 foil stack of aluminum with 1  $\mu\text{m}$  thick foils. The flux at peak height is 0.74 J/coulomb and the FWHM is 0.94 mm.

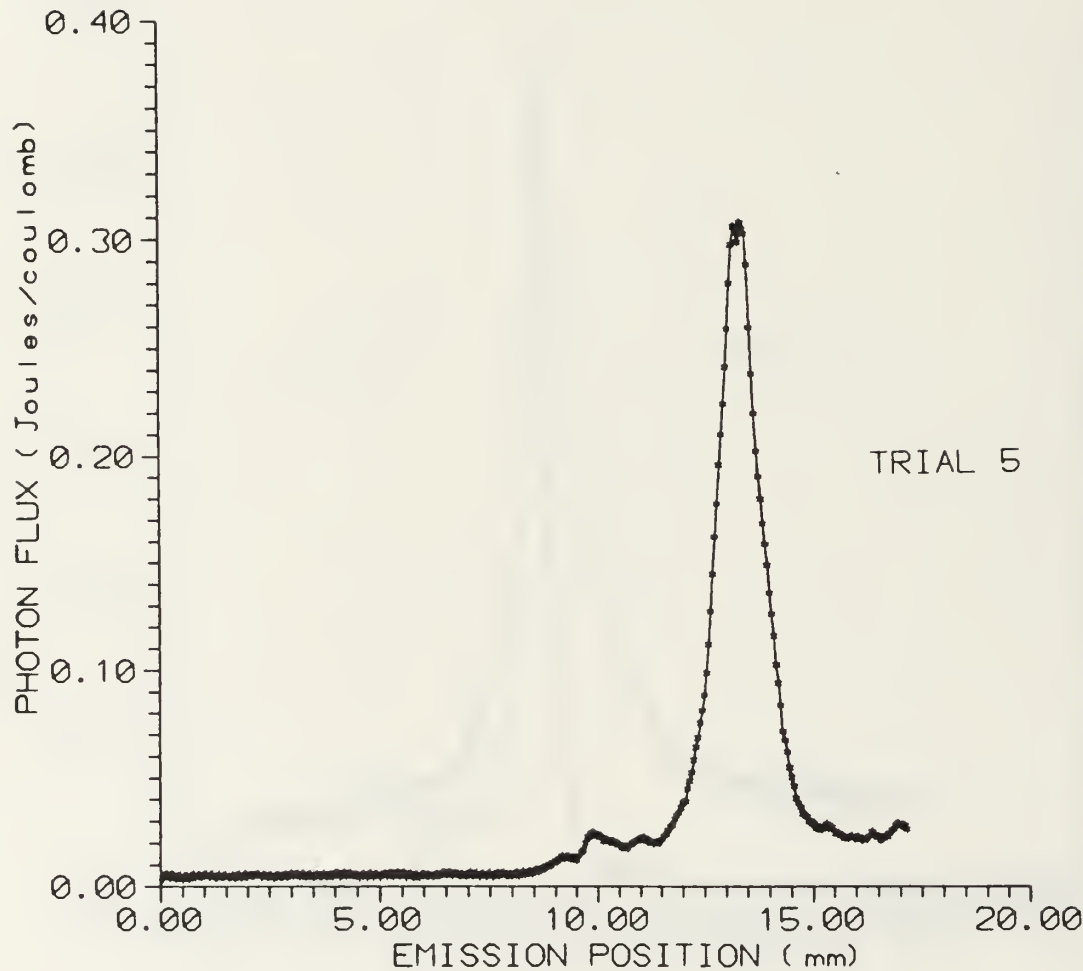


Figure 18. Measured 1-D emission profile of soft x-rays focused by a quartz elliptical optic. The soft x-rays were produced by a 65 MeV electron beam incident on a 10 foil stack of aluminum with 1  $\mu\text{m}$  thick foils. The flux at peak height is 0.31 J/coulomb and the FWHM is 1.19 mm.

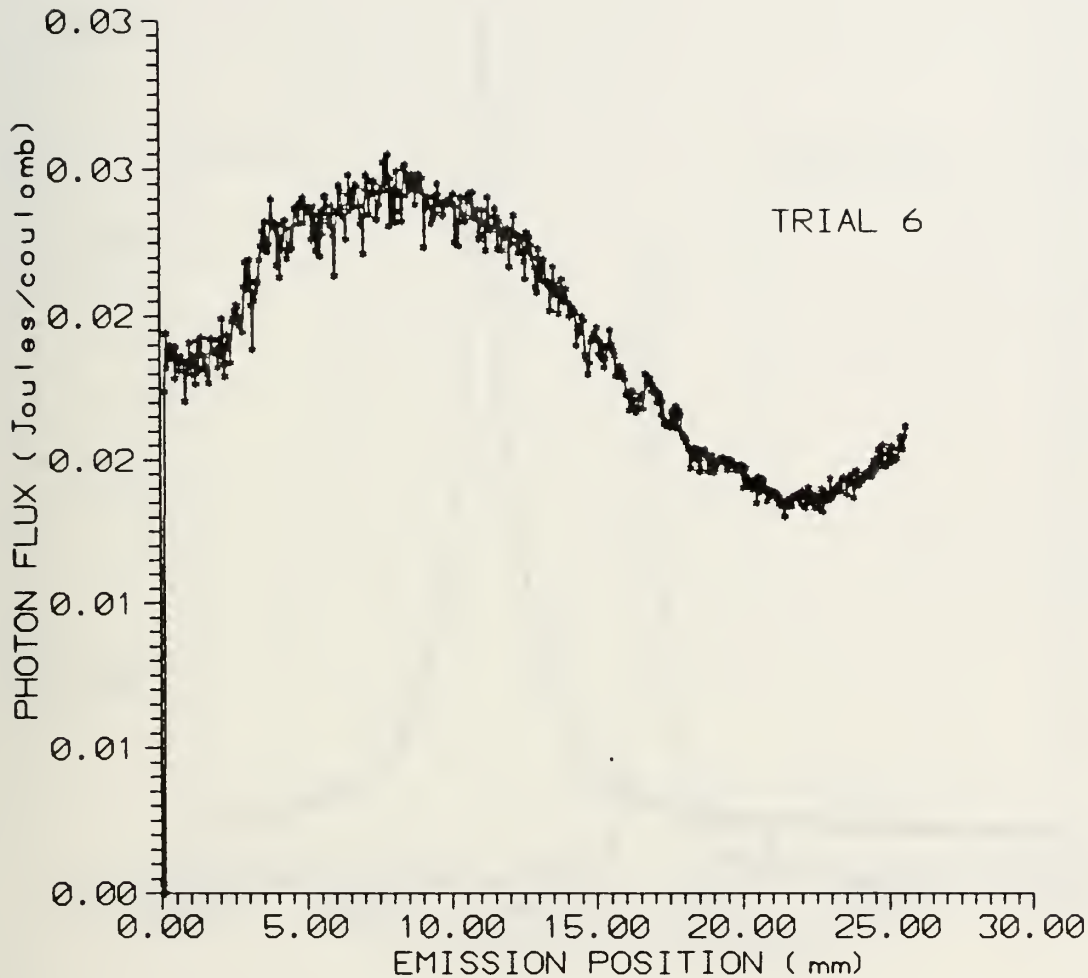


Figure 19. Measured 1-D emission profile of soft x-rays produced by an 89 MeV electron beam incident upon a 10 foil stack of aluminum with 1  $\mu$ m thick foils. No focusing optics present.

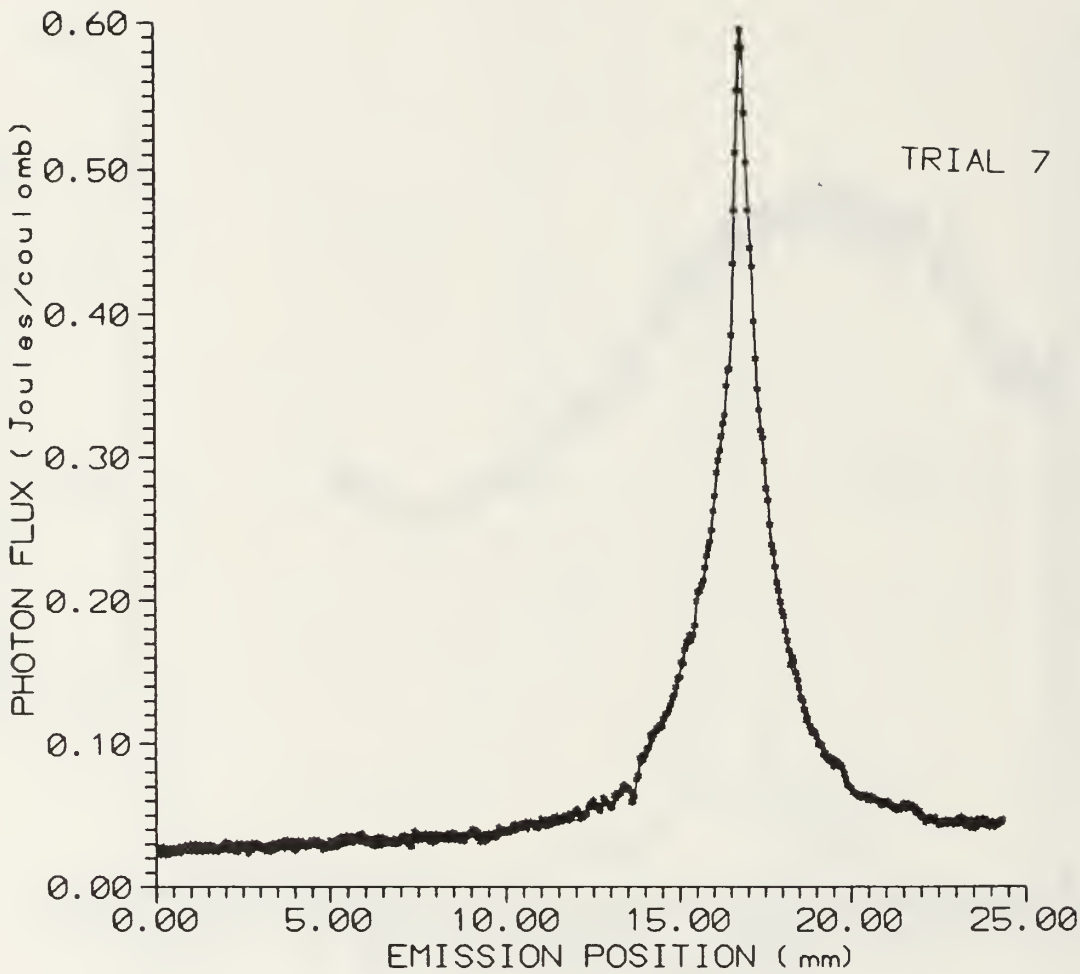


Figure 20. Measured 1-D emission profile of soft x-rays focused by a nickel elliptical optic. The soft x-rays were produced by a 96 MeV electron beam incident on a 10 foil stack of titanium with 1  $\mu\text{m}$  thick foils. The flux at peak height is 0.60 J/coulomb and the FWHM is 1.35 mm. Slits installed.

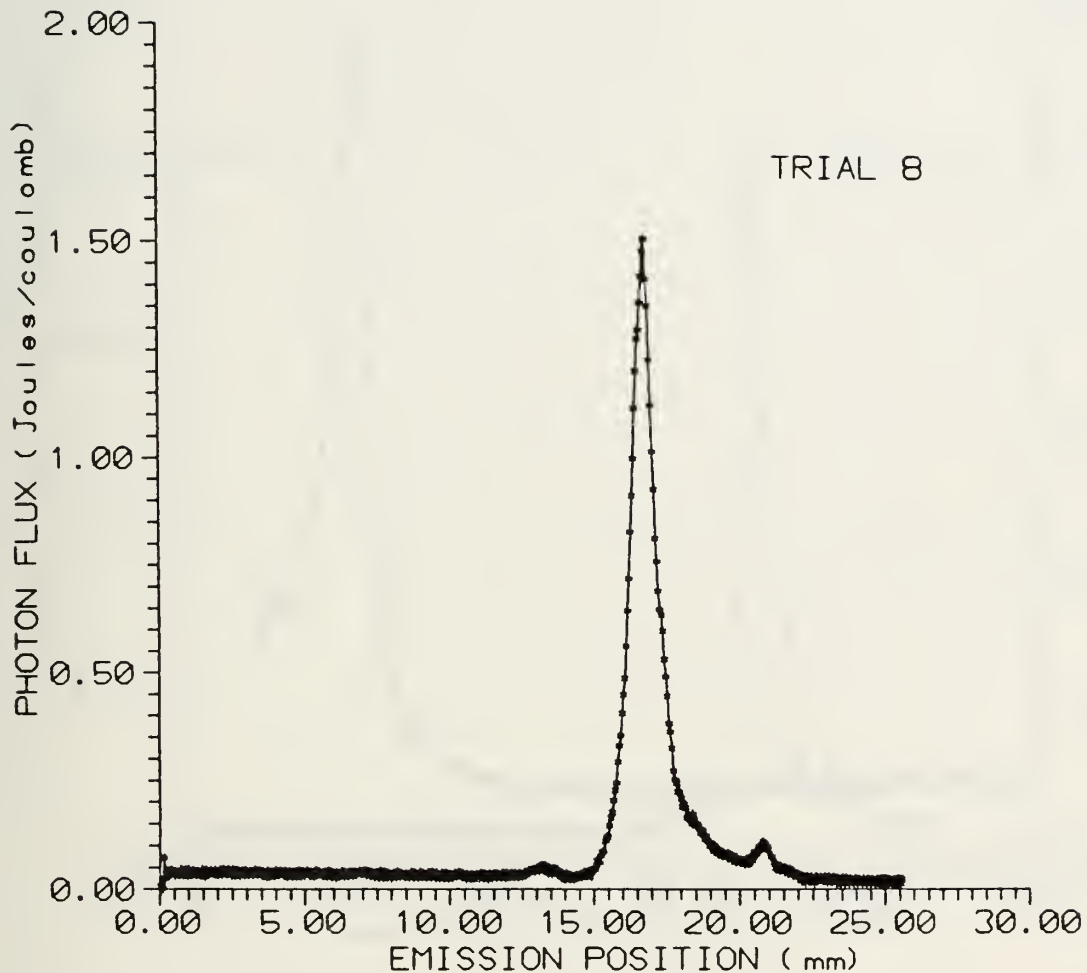


Figure 21. Measured 1-D emission profile of soft x-rays focused by a quartz cylindrical optic. The soft x-rays were produced by a 95 MeV electron beam incident on a 10 foil stack of titanium with 1  $\mu\text{m}$  thick foils. The flux at peak height is 1.50 J/coulomb and the FWHM is 0.93 mm. Slits installed.

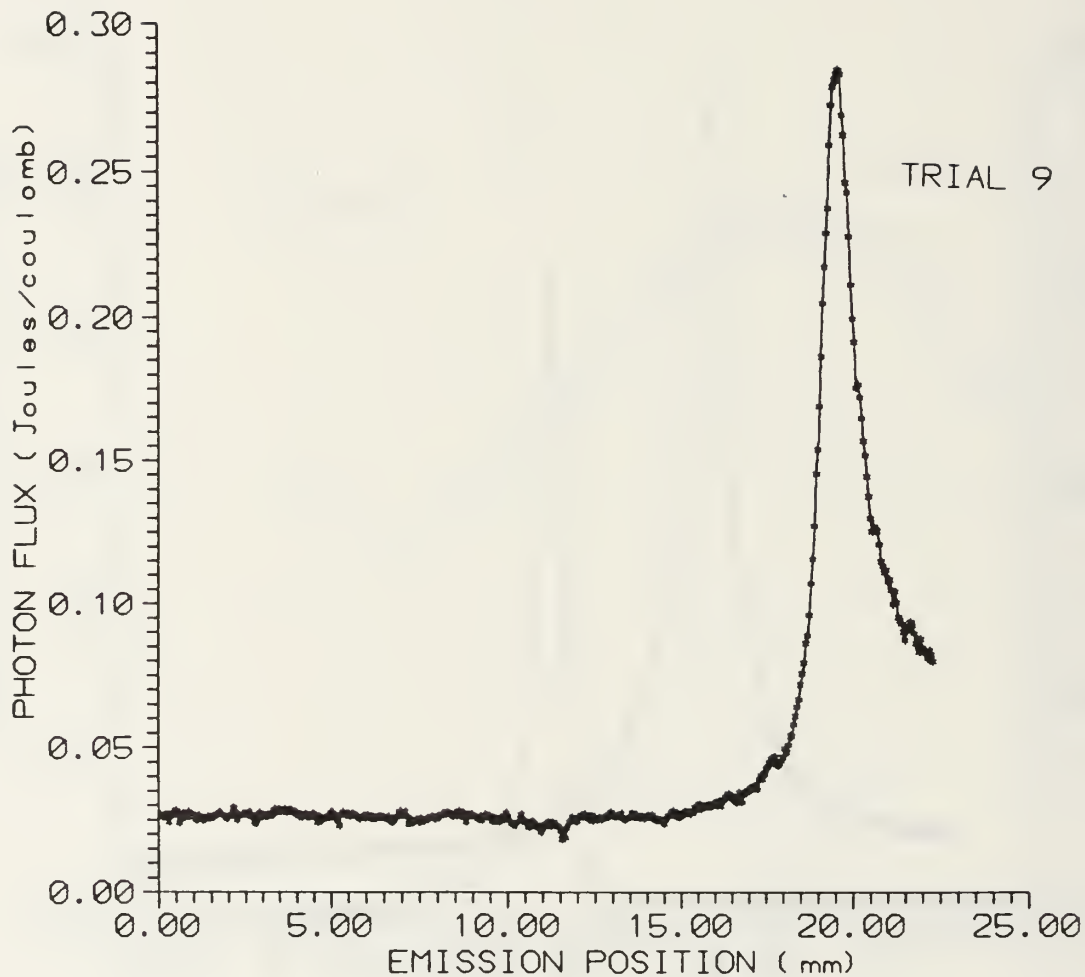


Figure 22. Measured 1-D emission profile of soft x-rays focused by a nickel elliptical optic. The soft x-rays were produced by a 95 MeV electron beam incident on a 10 foil stack of titanium with 1  $\mu\text{m}$  thick foils. The flux at peak height is .285 J/coulomb and the FWHM is 1.45 mm. Slits installed and 6.5  $\mu\text{m}$  of mylar was covering the entrance of the optic.

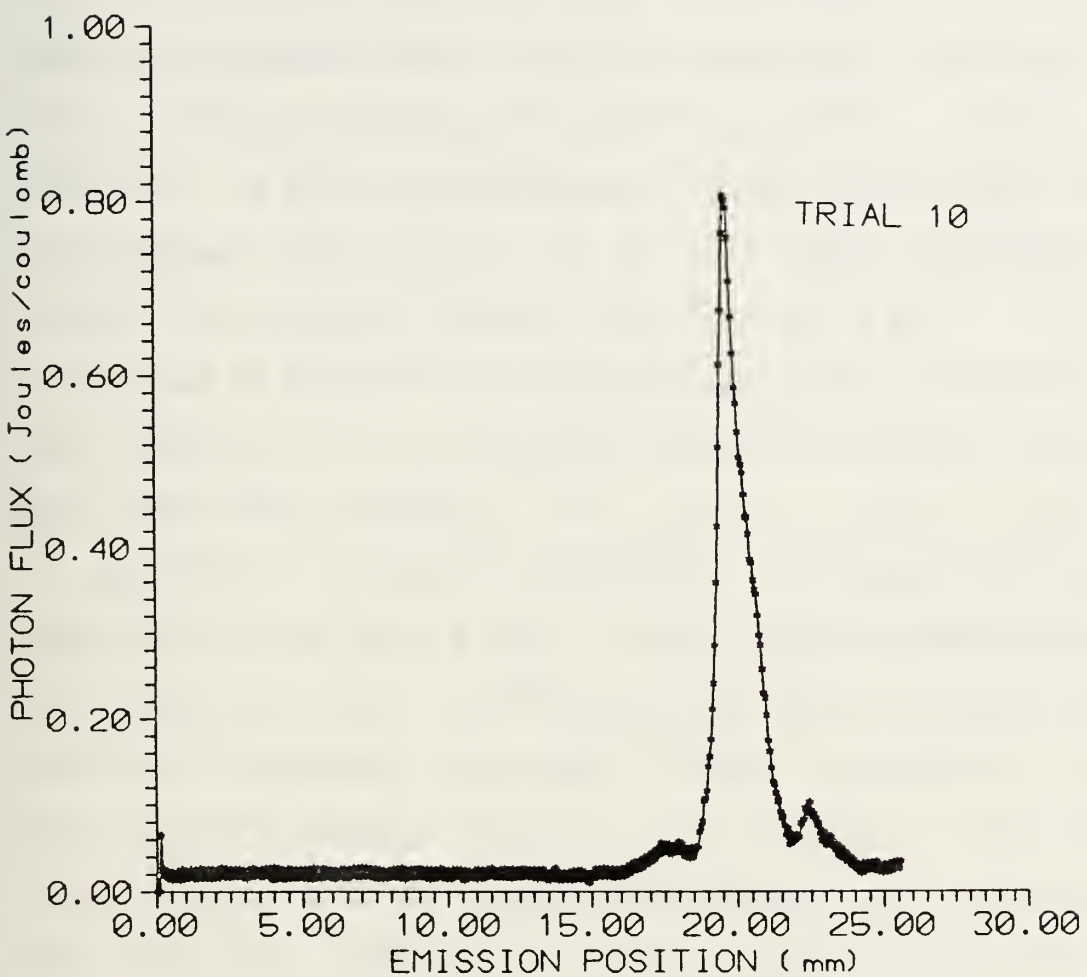


Figure 23. Measured 1-D emission profile of soft x-rays focused by a quartz cylindrical optic. The soft x-rays were produced by a 95 MeV electron beam incident on a 10 foil stack of titanium with 1  $\mu\text{m}$  thick foils. The flux at peak height is 0.82 J/coulomb and the FWHM is 1.05 mm. Slits installed and 6.5  $\mu\text{m}$  of mylar was covering the entrance of the optic.

## V. ANALYSIS

The data analysis presented in this paper is a graphical comparison of the intensity profiles displayed in Figures 14-23. Previous experiments [Ref. 6] have demonstrated the ability of the cylindrical optical focusing system to effectively focus the conically diverging pattern of TR. Based on the geometric properties of an ellipse, as presented in Chapter II, the elliptical optic should increase the overall intensity of the focal spot by one to two orders of magnitude. In order to determine if the results verify this theory, the profiles of the two optics with comparable electron beam energies were compared. Referring to Table III, the comparisons made were trials 3 and 5, 7 and 8, and 9 and 10. These comparisons are shown in Figures 24-26. At first glance the quartz cylindrical optic indicates apparently superior performance. However, upon further analysis it will be demonstrated that, assuming equivalent surface roughness, the nickel elliptical optic actually collected 3-5 times more energy.

### A. OPTIC LOSSES

Before an accurate comparison of the above intensity profiles can be made, the total reflectivity, as given by the product of equations 2.12 and 2.13, must be calculated. As

previously discussed  $R_p=1$  as long as the angle of incidence is less than the critical angle of reflection. Table IV summarizes the maximum values of soft x-ray energy, for the two optics at various beam energies, to insure that the critical angle is not exceeded. For example, intensity profile #1 (Figure 14) is from a beam energy of 85 MeV and a nickel optic with plasma a frequency,  $\omega_p$ , of 59.4 eV. Using equation 1.5, this yields an optimum angle of incidence of 6 mrad. In order for this to be less than the critical angle of reflection, as given by equation 2.2, the energy of the soft x-rays,  $\omega$ , has to be less than 9.9 keV.

Figures 27-31 show the dependence of equation 2.13 to the wavelength of the soft x-rays. It is easily seen that below a wavelength of .4 nm (above 3 keV) the reflectivity is approximately zero for all cases. However, Figures 14-23 all show a focused intensity profile. It follows that the energy of the x-rays that the optics were able to focus had to be less than 3 keV. Referring to Table IV, we see that 3 keV is below the maximum x-ray energy that will insure the angle of incidence is less than the critical angle of reflection. Therefore  $R_p=1$ , and the total reflectivity is given by equation 2.13 and graphically represented by Figures 27-31.

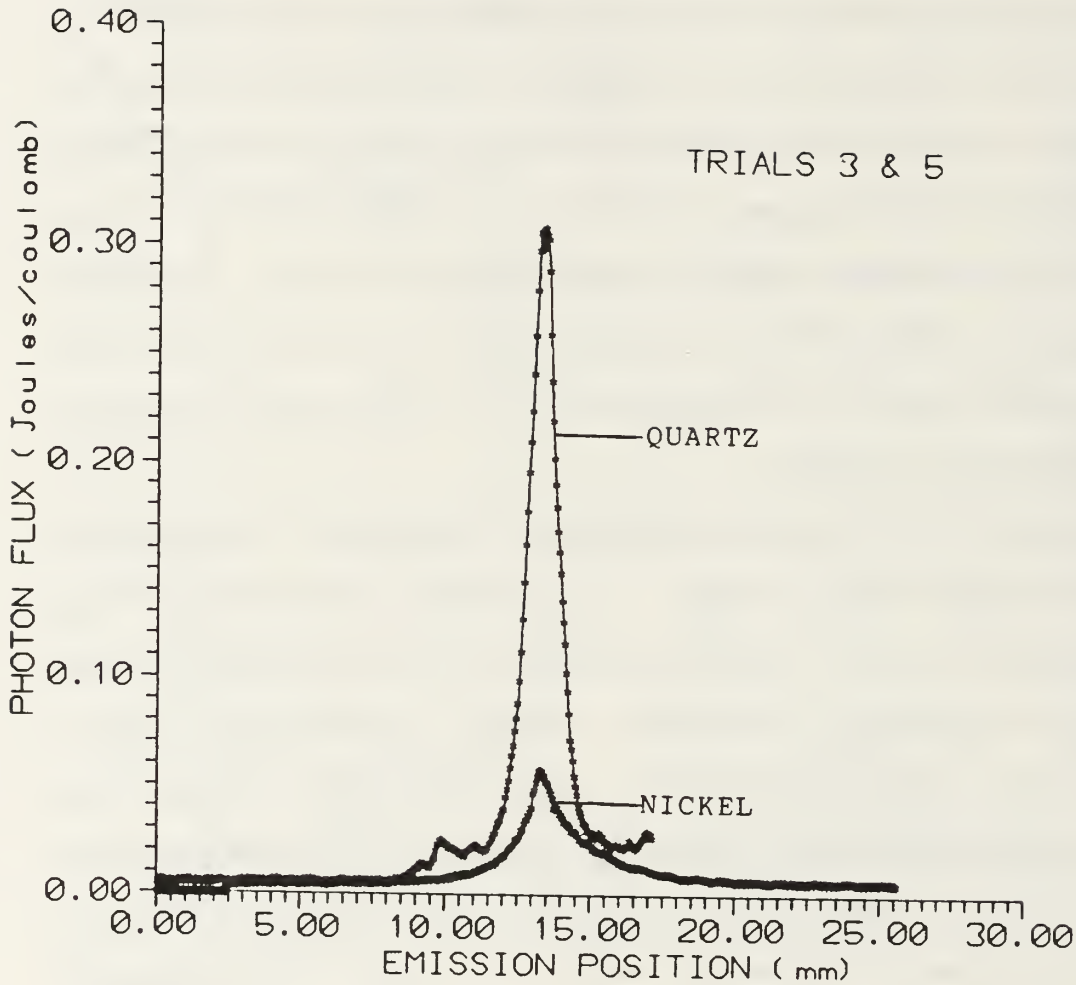


Figure 24. Comparison of intensity profiles from a nickel elliptical optic with an electron beam energy of 61 MeV and a quartz cylindrical optic with an electron beam energy of 65 MeV. The elliptical optic has a peak flux of .058 J/coulomb, a FWHM of 1.82 mm, and collected .155 J/coulomb between +/- 3.5 mm of peak compared to a peak flux of .31 J/coulomb, a FWHM of 1.19 mm, and .511 J/coulomb collected between +/- 3.5 mm of peak for the cylindrical optic.

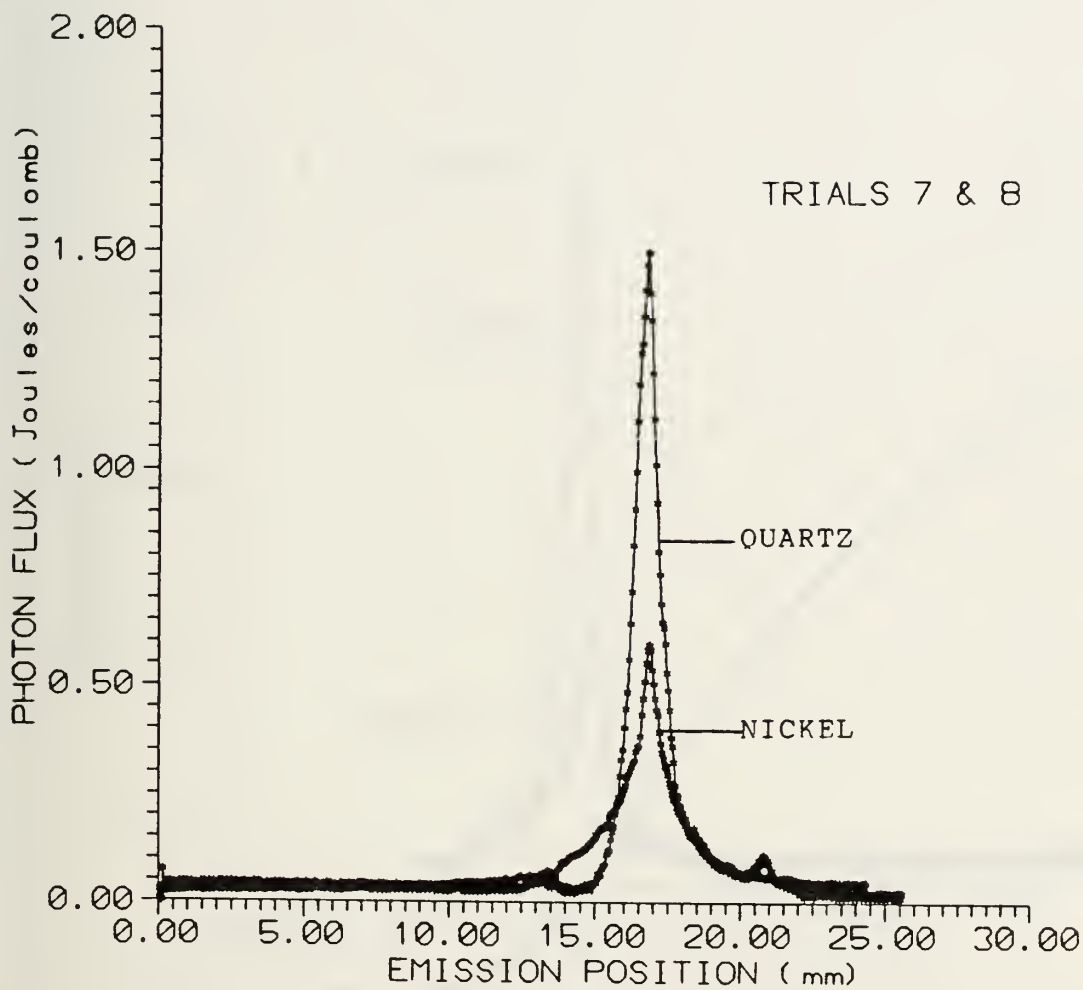


Figure 25. Comparison of intensity profiles from a nickel elliptical optic with an electron beam energy of 96 MeV and a quartz cylindrical optic with an electron beam energy of 95 MeV. The elliptical optic has a peak flux of 0.60 J/coulomb, a FWHM of 1.35 mm, and collected 1.33 J/coulomb between  $\pm$  3.5 mm of peak compared to a peak flux of 1.5 J/coulomb, a FWHM of .93 mm, and 2.04 J/coulomb collected between  $\pm$  3.5 mm of peak for the cylindrical optic.

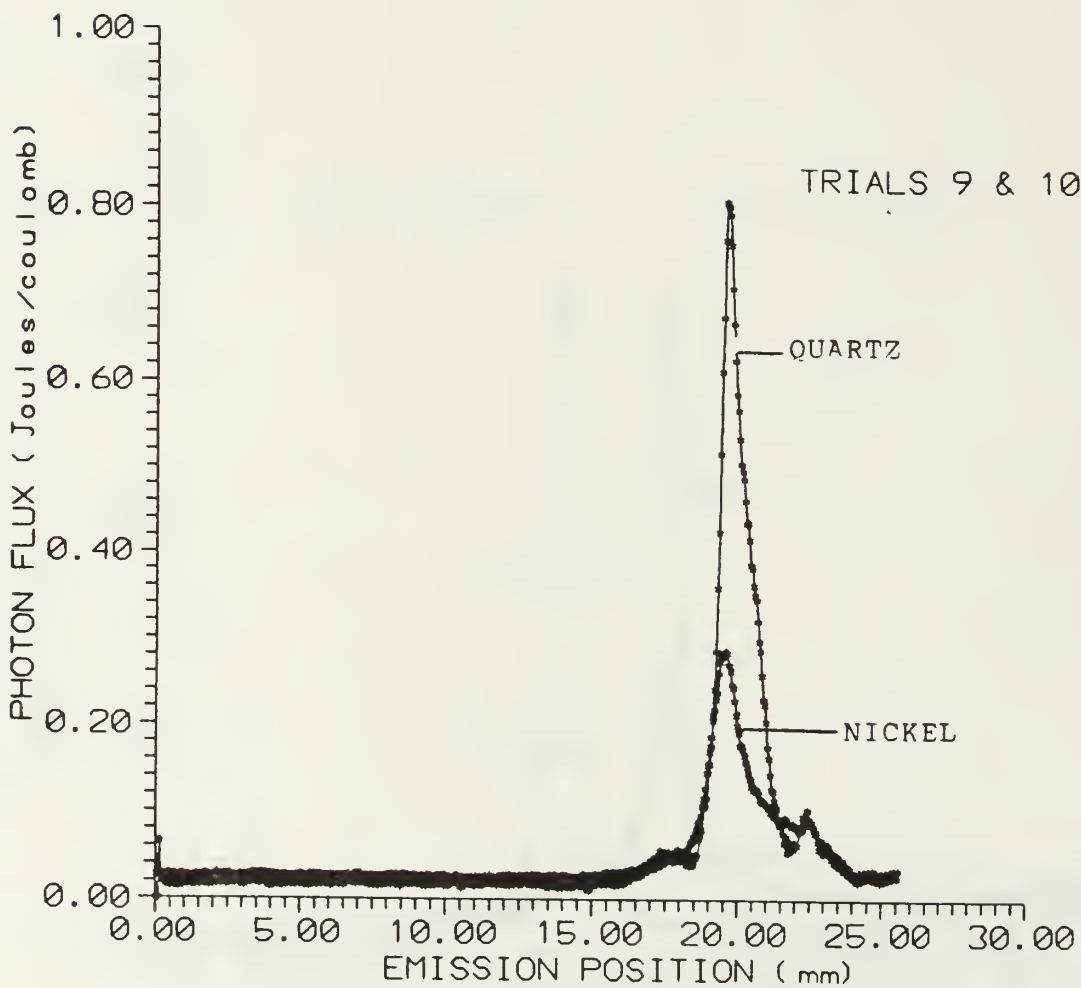


Figure 26. Comparison of intensity profiles from a nickel elliptical optic with an electron beam energy of 95 MeV and a quartz cylindrical optic with an electron beam energy of 95 MeV. The optics had 6.5  $\mu\text{m}$  of mylar covering their entrance. The elliptical optic has a peak flux of .285 J/coulomb, a FWHM of 1.45 mm, and collected 0.65 J/coulomb between  $\pm$  3.5 mm of peak compared to a peak flux of .82 J/coulomb, a FWHM of 1.0 mm, and 1.22 J/coulomb collected between  $\pm$  3.5 mm of peak for the cylindrical optic.

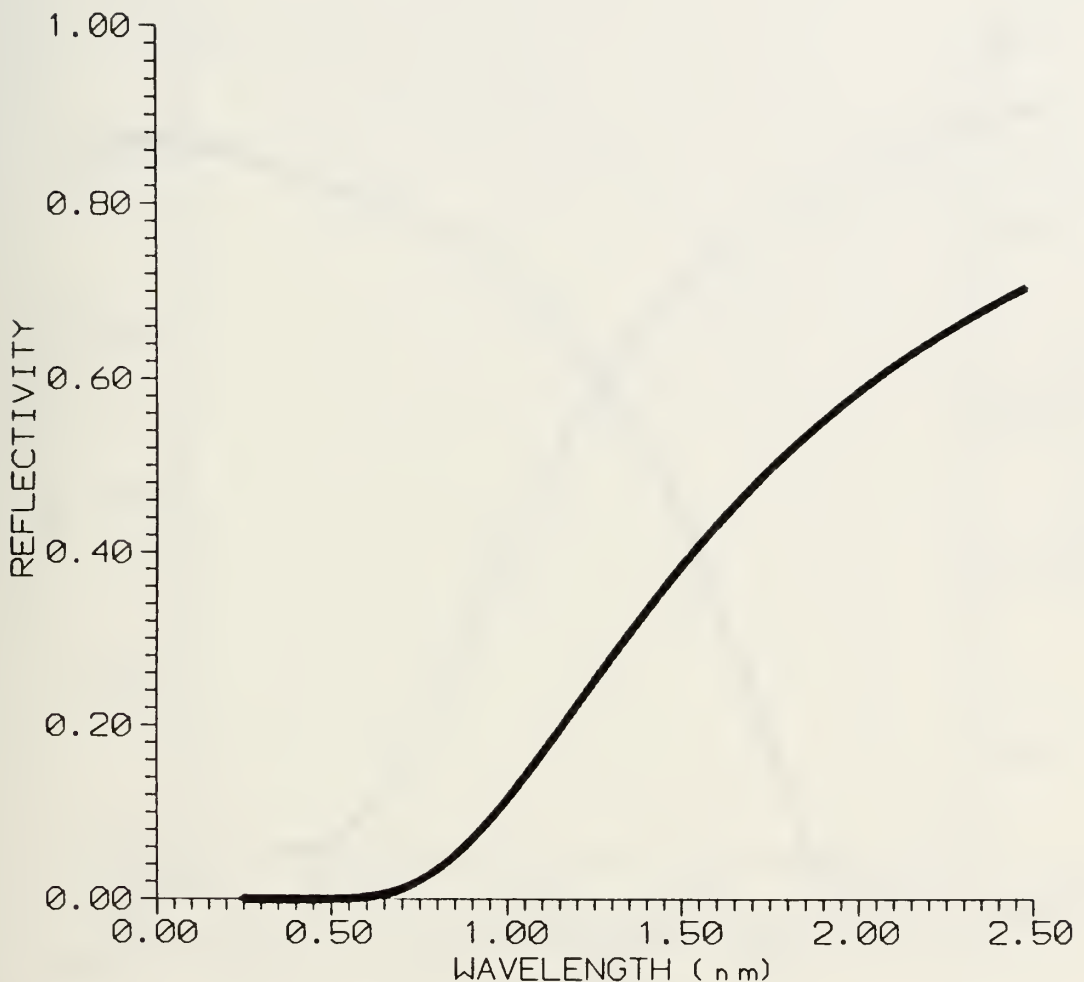


Figure 27. Reflectivity of nickel elliptical optic, as given by equation 2.13, with an electron beam energy of 61 MeV over a soft x-ray wavelength range of .248 nm (5 keV) to 2.48 nm (500 eV).

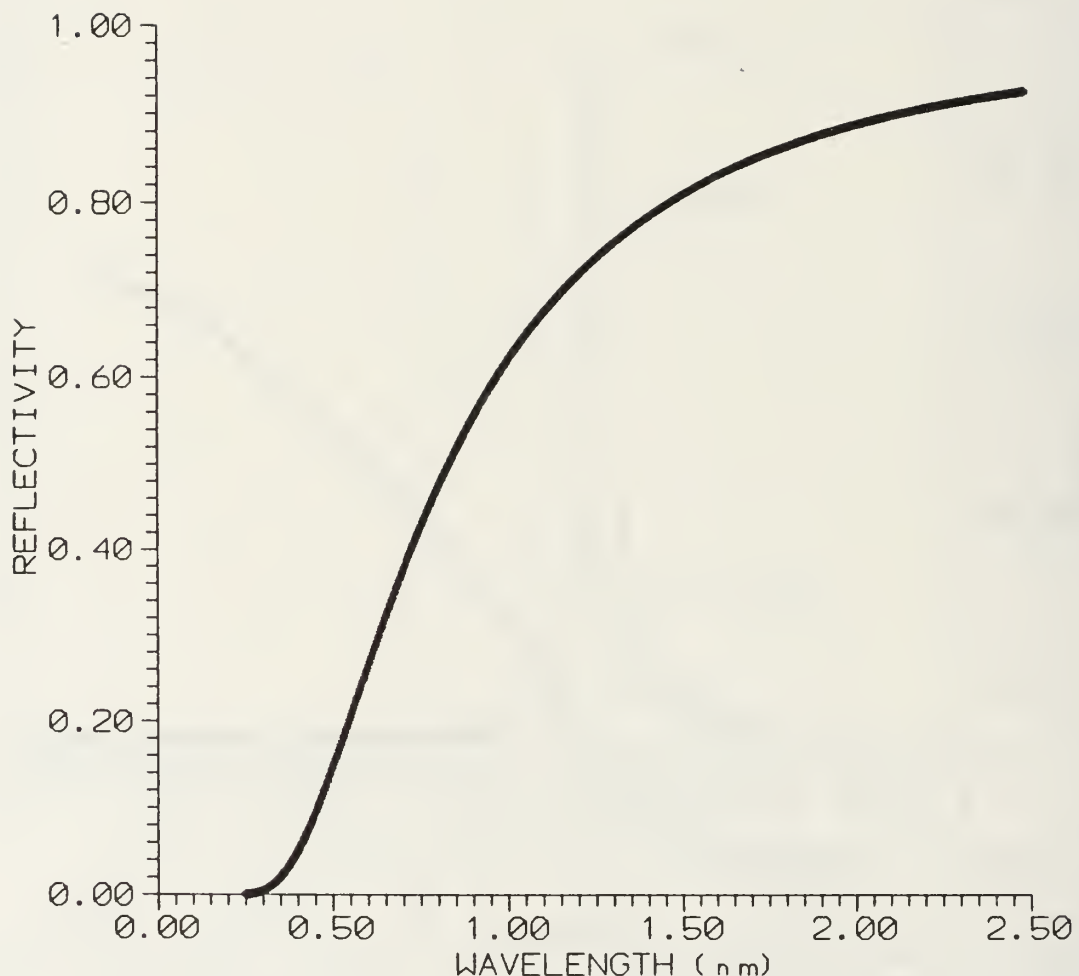


Figure 28. Reflectivity of quartz cylindrical optic, as given by equation 2.13, with an electron beam energy of 65 MeV over a soft x-ray wavelength range of .248 nm (5 kev) to 2.48 nm (500 eV).

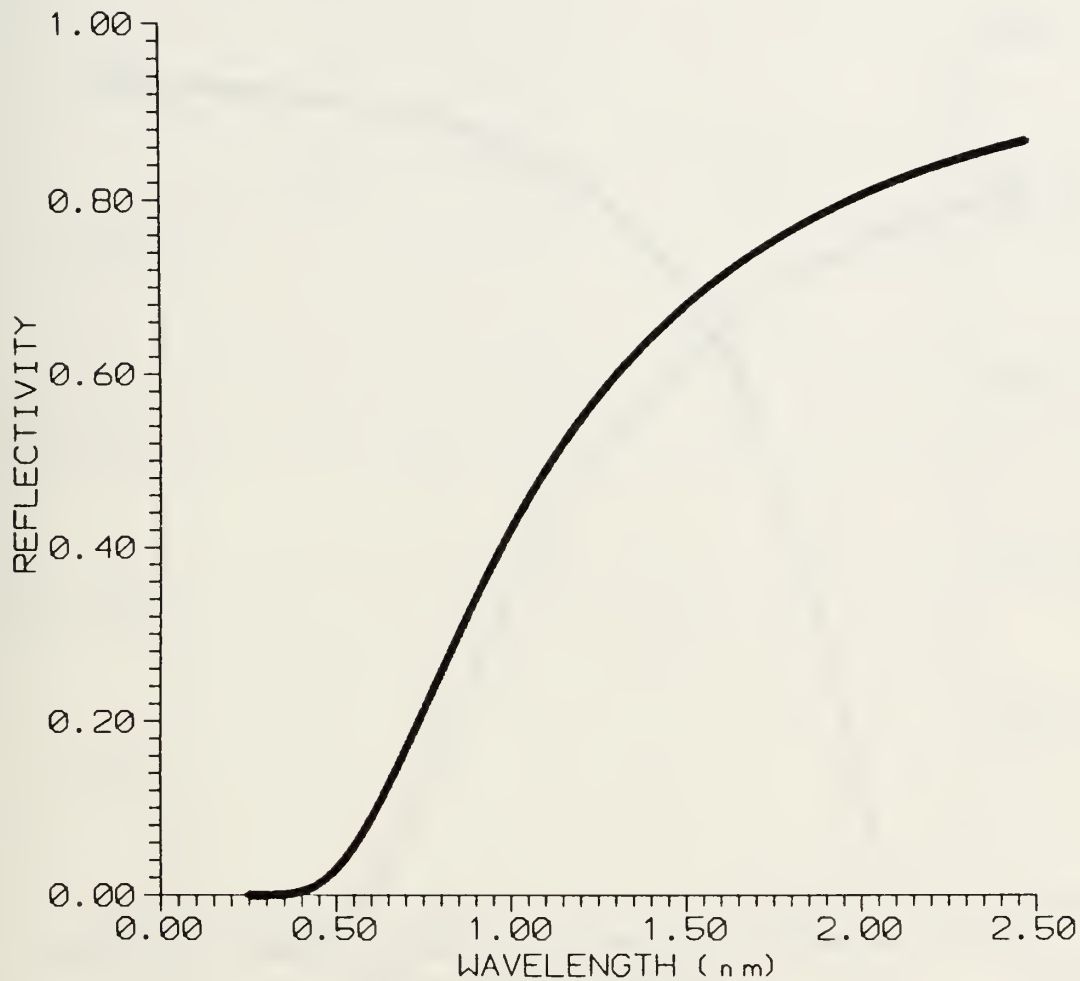


Figure 29. Reflectivity of nickel elliptical optic, as given by equation 2.13, with an electron beam energy of 96 MeV over a soft x-ray wavelength range of .248 nm (5 keV) to 2.48 nm (500 eV).

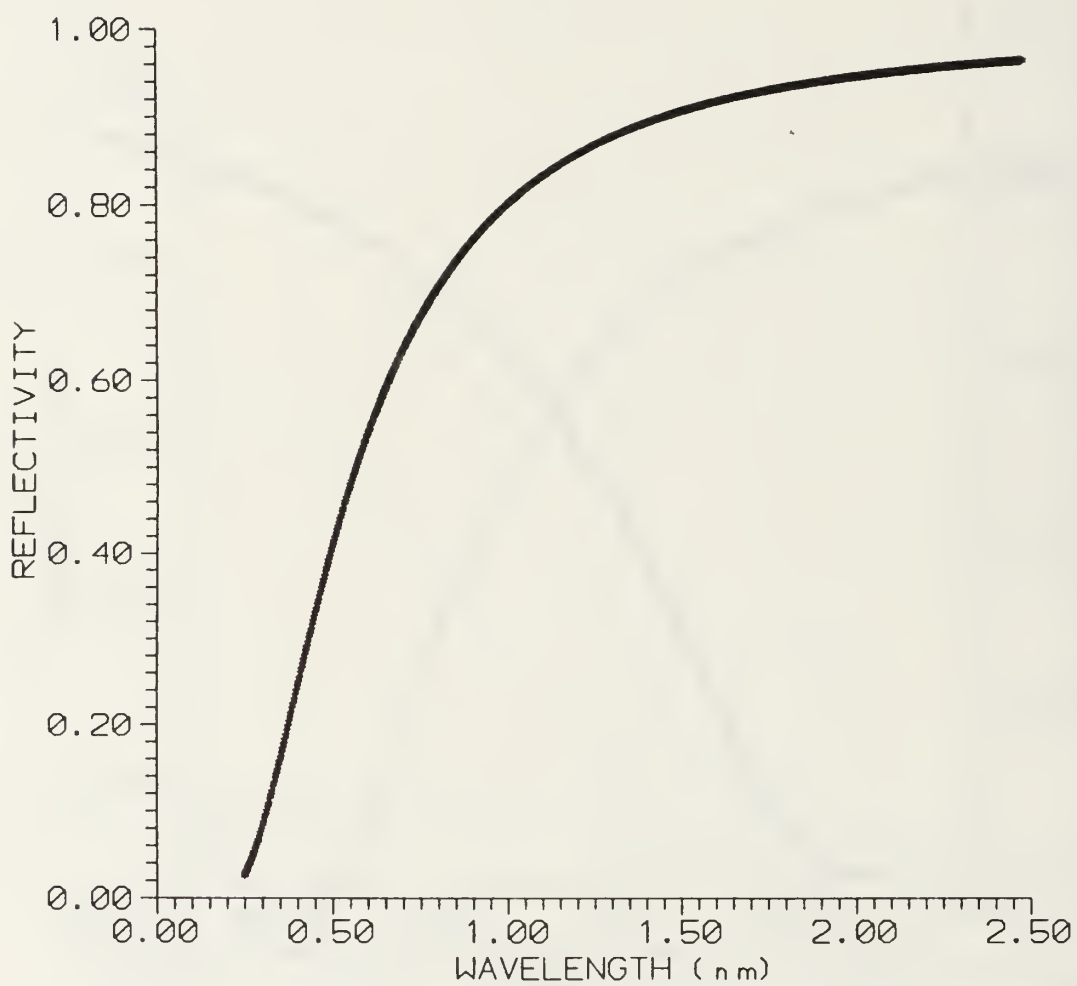


Figure 30. Reflectivity of quartz cylindrical optic, as given by equation 2.13, with an electron beam energy of 95 MeV over a soft x-ray wavelength range of .248 nm (5 keV) to 2.48 nm (500 eV).

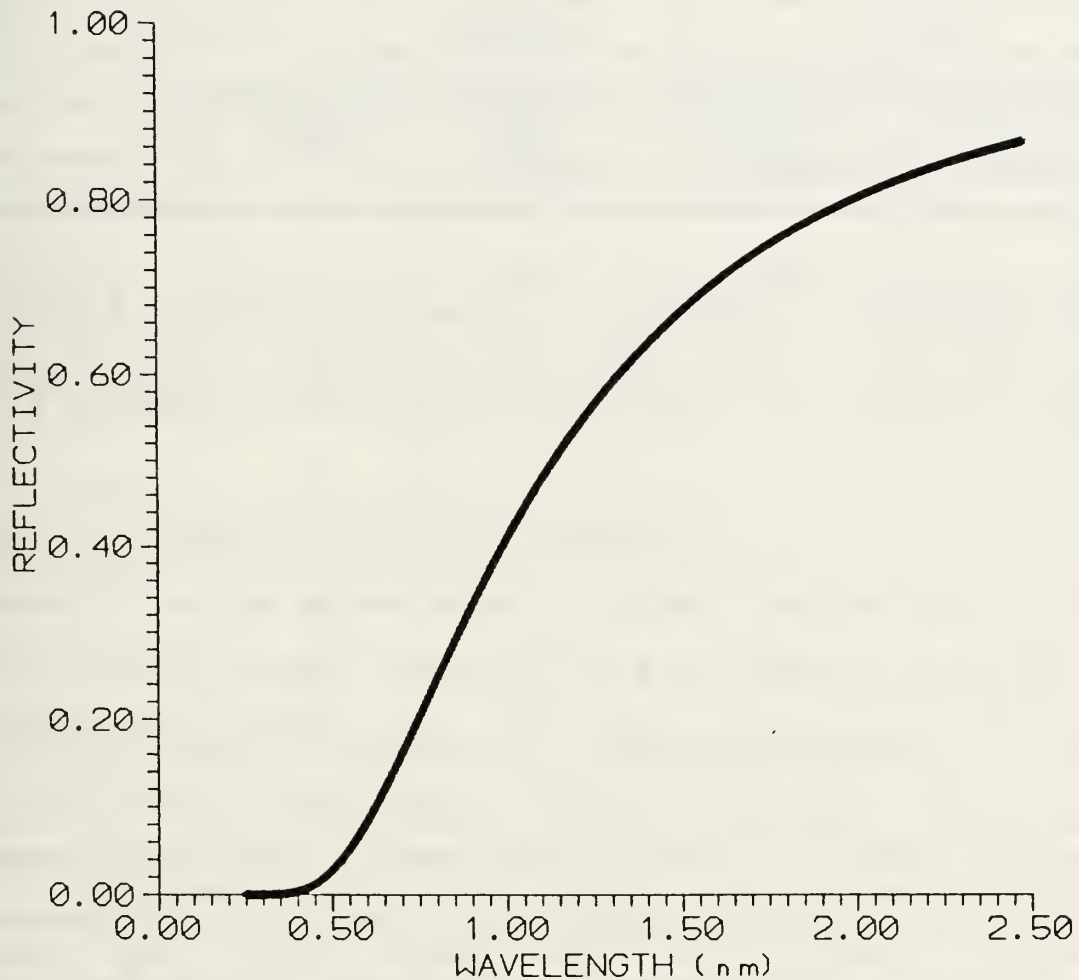


Figure 31. Reflectivity of nickel elliptical optic, as given by equation 2.13, with an electron beam energy of 95 MeV over a soft x-ray wavelength range of .248 nm (5 keV) to 2.48 nm (500 eV).

TABLE IV

Electron Beam Energy (MeV)	Quartz E <sub>MAX</sub> (keV)	Nickel E <sub>MAX</sub> (keV)
85	5.53	9.90
61	3.95	7.07
92	5.93	10.61
65	4.20	7.52
96	6.26	11.21
95	6.15	11.00

$E_{MAX}$  represents the maximum energy of soft x-rays to insure that the angle of incidence, as given by equation 1.5, does not exceed the critical angle of reflection, as given by equation 2.2, for the two optics at the electron beam energies used in the three comparisons shown in Figures 24-26.

Increased surface roughness causes an increased variation of reflection angles, thereby a larger energy spread at focus. The surface roughness of the nickel and quartz optics is 14 and 7 nm respectively [Ref. 12], which makes this effect significant. Therefore, in order to determine how much energy each optic actually collected, the intensity profiles between  $\pm 3.5$  mm of the peak intensity were numerically integrated, and the results are presented in Table V. The cylindrical optic still seems to have superior performance, however the surface roughness loss must be numerically taken into account. Figures 32-34 show graphical representations of the reflectiv-

ity of the nickel optic divided by the reflectivity of the quartz optic, ranging from .248 nm (5 keV) to 2.48 nm (500 eV), for the three comparisons made. Again, the reflectivities were determined from equation 2.13.

TABLE V

	Beam Energy (MeV)	Measured Flux (J/coulomb)	Reflectivity Ratio (Nickel/Quartz)	Corrected Flux (J/coulomb)
Figure 24: Trial 3 (Nickel Optic)	61	.155	.064	2.42
Trial 5 (Quartz Optic)	65	.511		.511
Figure 25: Trial 7 (Nickel Optic)	96	1.33	0.18	7.39
Trial 8 (Quartz Optic)	95	2.04		2.04
Figure 26: Trial 9 (Nickel Optic)	95	0.65	0.17	3.82
Trial 10 (Quartz Optic)	95	1.22		1.22

Table V. Flux collected by optics. Column 1 shows the electron beam energy used in each trial. Column 2 shows the total integrated flux between  $\pm 3.5$  mm of peak height. Column 3 shows the ratio of reflectivity of the nickel optic to the quartz optic for the given electron beam energies. Column 4 shows the flux collected by the nickel optic divided by the ratio of reflectivity compared to the flux collected by the quartz optic. Trials 3 and 5 assume a 1.56 keV dominance of x-rays whereas trials 7-10 assume a 2 keV dominance. In trials 9 and 10, 6.5  $\mu\text{m}$  of mylar were covering entrance of optics.

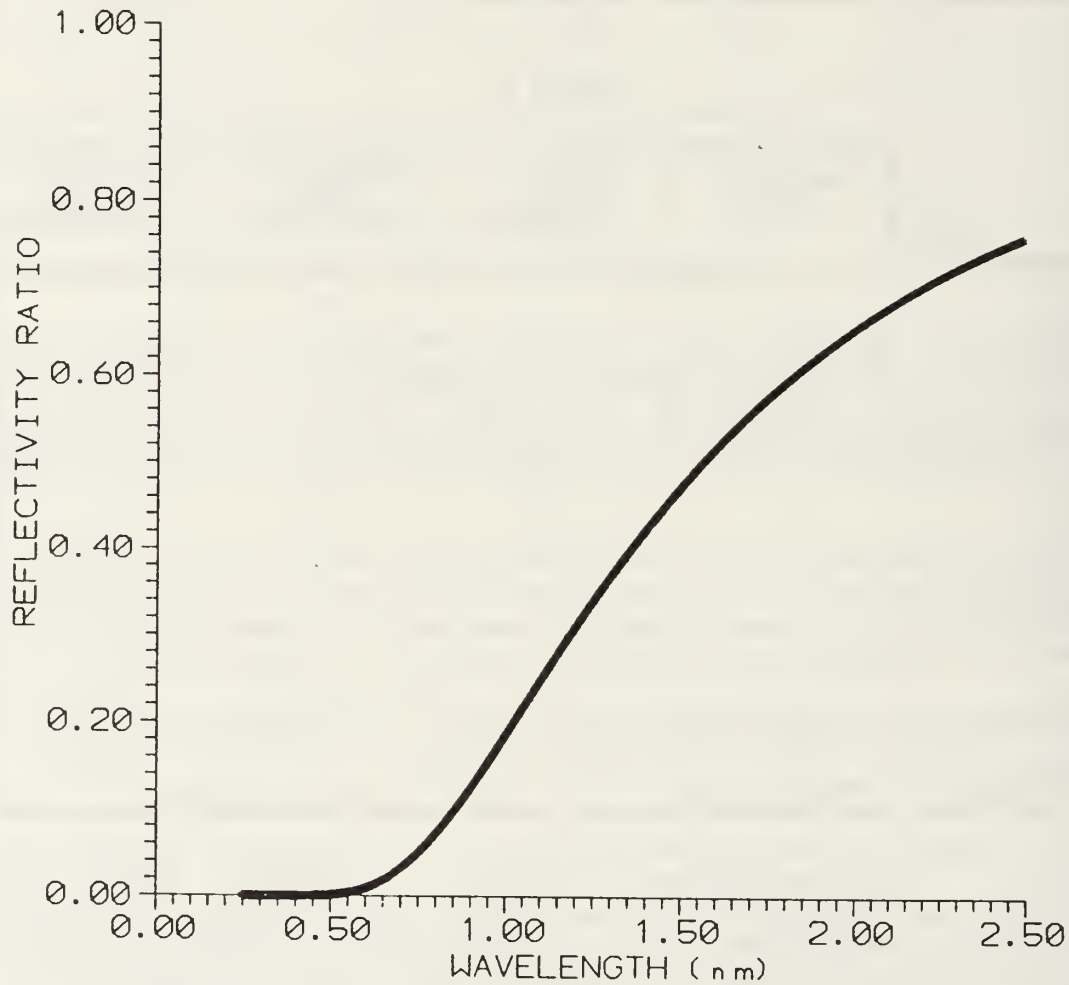


Figure 32. Ratio of reflectivity of nickel elliptical optic with electron beam energy of 61 MeV to the reflectivity of the quartz cylindrical optic with electron beam energy of 65 MeV over range of soft x-rays from .248 nm (5 keV) to 2.48 nm (500 keV).

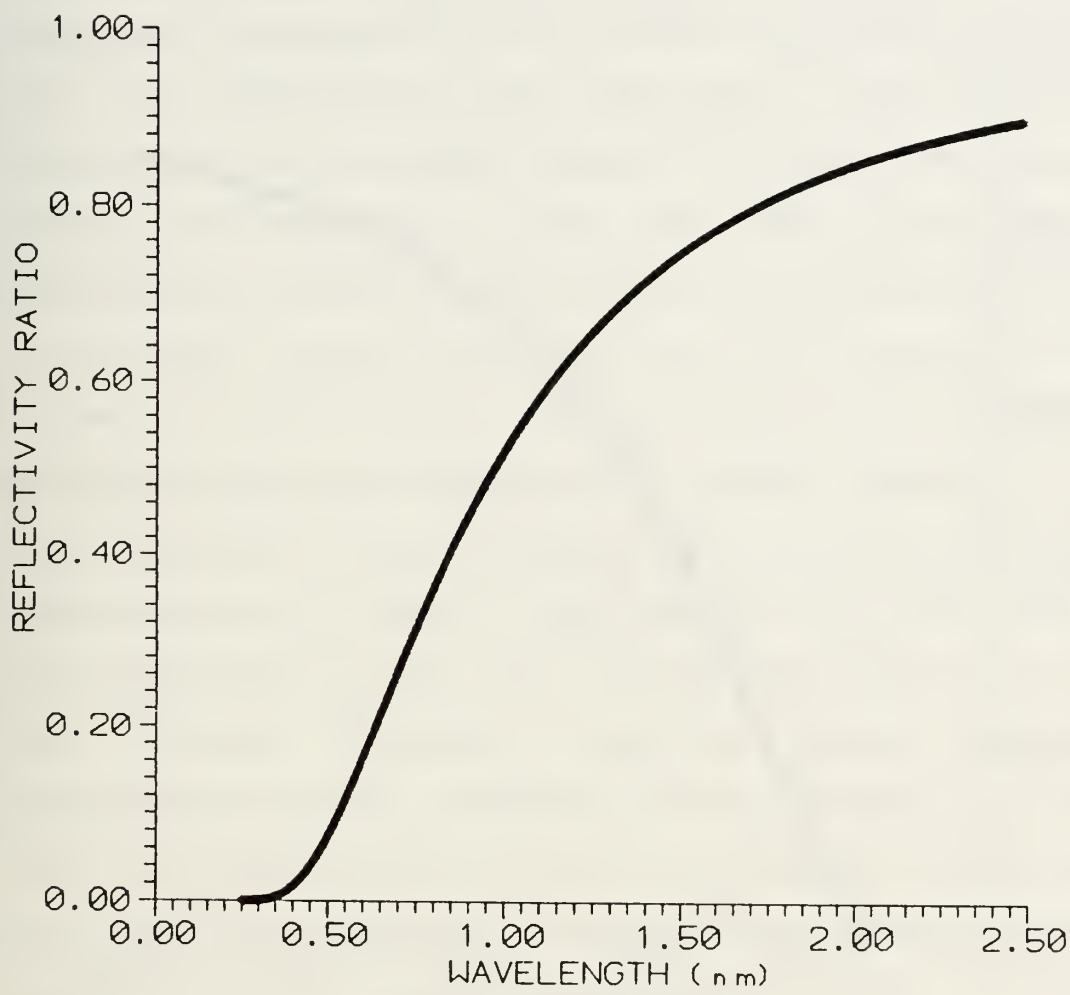


Figure 33. Ratio of reflectivity of nickel elliptical optic with electron beam energy of 96 MeV to the reflectivity of the quartz cylindrical optic with electron beam energy of 95 MeV over range of soft x-rays from .248 nm (5 keV) to 2.48 nm (500 keV).

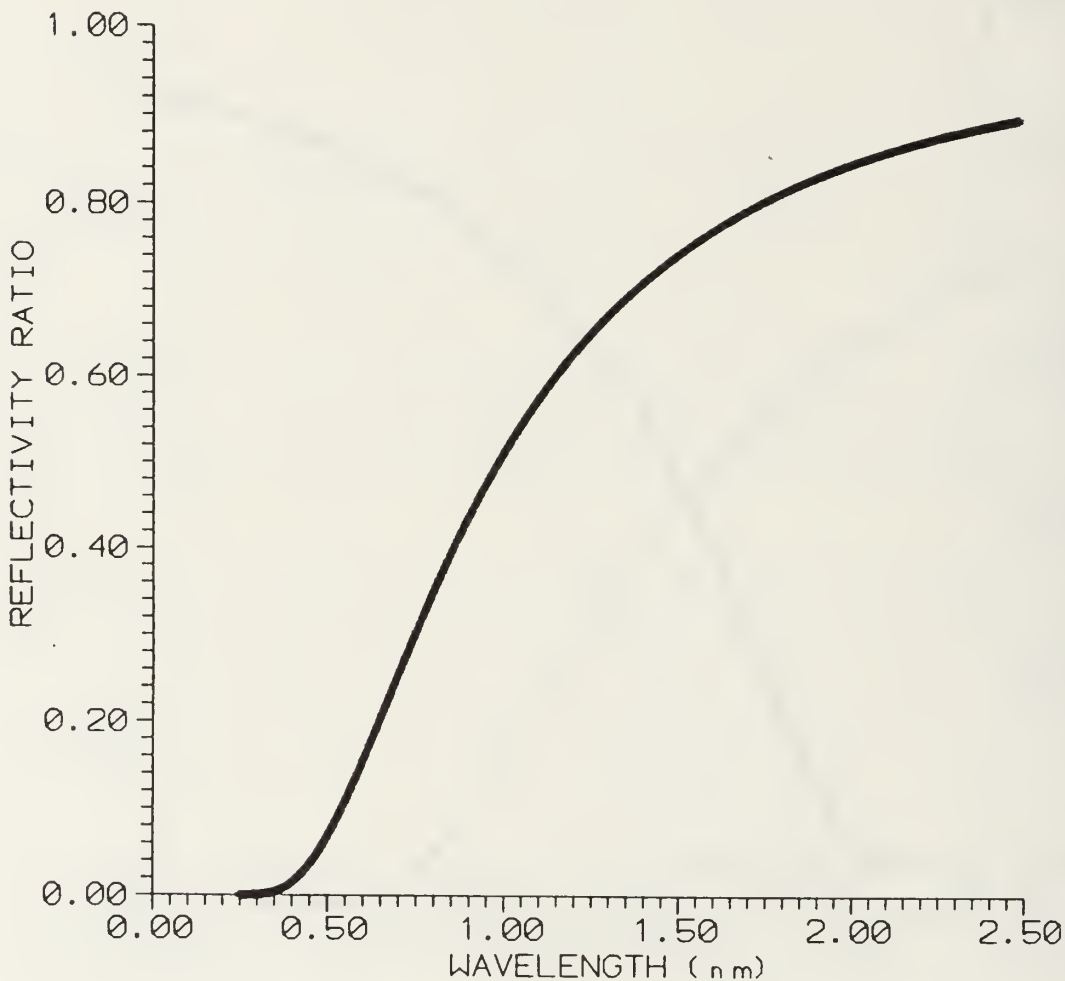


Figure 34. Ratio of reflectivity of nickel elliptical optic with electron beam energy of 95 MeV to the reflectivity of the quartz cylindrical optic with electron beam energy of 95 MeV over range of soft x-rays from .248 nm (5 keV) to 2.48 nm (500 keV).

The foil stacks are designed to emit photons at their K-edge frequencies [Ref. 16], therefore it is assumed the soft x-rays produced were dominated by photons at these energies. The K-edge of aluminum is given by [Ref. 16] as 1.56 keV (0.8 nm). The aluminum foil stack was used in trials 3 (nickel optic) and 5 (quartz optic) and their corresponding intensity profiles are compared in Figure 24. The reflectivity of nickel with an electron beam energy of 61 MeV (beam energy in trial 3) for 1.56 keV x-rays is .03 as given by equation 2.13. The reflectivity of quartz with an electron beam energy of 65 MeV (beam energy in trial 5) for 1.56 keV x-rays is .47 as given by equation 2.13. Therefore, the reflectivity ratio (nickel/quartz) is .064. From Table V we see that the integrated flux in trial 3 is .155 J/coulomb and in trial 5 is .511 J/coulomb. In order to make an accurate comparison, independent of surface roughness, the integrated flux in trial 3 must be divided by the reflectivity ratio calculated above. This yields 2.42 J/coulomb collected in trial 3 (nickel optic) compared to .511 J/coulomb collected in trial 5 (quartz optic). This is almost a factor of five more flux collected by the nickel elliptical optic (see Table V).

Trials 7-10 were done using a titanium foil stack. The K-edge of titanium is 5 keV [Ref. 16]. However, Figures 27-31 show that the reflectivity of both optics is zero at a

wavelength of 0.248 nm (5 keV). Specifically, Figures 27, 29, and 30 show that the reflectivity is zero below a wavelength of 0.4 nm (3 keV). However, the corresponding intensity profiles exhibit a focus. Therefore, when comparing intensity profiles obtained using the titanium foil stack, a soft x-ray energy below 3 keV must be assumed. Taking this into account, along with previous measurements of the spectral photon density for titanium [Ref. 17], it is assumed that the soft x-rays generated from the titanium foil stack were dominated by 2 keV photons.

The comparison of trials 7 (nickel optic) and 8 (quartz optic) is shown in Figure 25. The reflectivity of nickel with an electron beam energy of 96 MeV (beam energy in trial 7) for 2 keV x-rays is .10 as given by equation 2.13. The reflectivity of quartz with an electron beam energy of 95 MeV (beam energy in trial 8) for 2 keV x-rays is .56 as given by equation 2.13. Therefore, the reflectivity ratio (nickel/quartz) is .18. From Table V we see that the integrated flux in trial 7 is 1.33 J/coulomb and in trial 8 is 2.04 J/coulomb. Dividing the integrated flux in trial 7 by the reflectivity ratio, 7.39 J/coulomb for the nickel elliptical optic is obtained (see Table V). This is approximately 3.5 times more flux collected by the nickel optic than the 2.04 J/coulomb that was collected by the quartz optic. The comparison of

trials 9 (nickel optic) and 10 (quartz optic) is shown in Figure 26. The reflectivity of nickel with an electron beam energy of 95 MeV (beam energy in trial 9) for 2 keV x-rays is .097 as given by equation 2.13. The reflectivity of quartz with an electron beam energy of 95 MeV (beam energy in trial 10) for 2 keV x-rays is .56 as previously determined. Therefore, the reflectivity ratio (nickel/quartz) is .17. From Table V we see that the integrated flux in trial 9 is 0.65 J/coulomb and in trial 10 is 1.22 J/coulomb. Dividing the integrated flux in trial 9 by the reflectivity ratio, 3.82 J/coulomb is obtained (see Table V). This is approximately 3 times more flux collected by the nickel optic than the 1.22 J/coulomb that was collected by the quartz optic.

#### B. EFFECTS OF MYLAR

The intensity profiles compared in Figure 26 were produced with 6.5 microns of mylar covering the entrance of the optics. It was originally assumed that the reflectivity of the optics would improve with shorter wavelength x-rays, and therefore an attempt was made to filter out the longer wavelength x-rays. However, as can be seen from Figures 27-31, this assumption was wrong. The reflectivity of the optics is better with longer wavelength x-rays.

One piece of information that can be extracted from the use of mylar is to help determine what energy of soft x-rays is dominant in the TR produced from the titanium foil stack. As previously mentioned, a 2 keV dominance was originally assumed. Furthermore, it has been shown that the reflectivity above 3 keV is approximately zero, and therefore is the upper limit of the soft x-ray energy that was focused. In order to determine the lower limit, the attenuation due to the mylar is calculated in the range 0.1-5 keV. From [Ref. 18]:

$$I = I_0 e^{-\mu x}$$

where  $\mu$  is the x-ray attenuation coefficient of mylar [Ref. 19], and  $x$  is the thickness of the mylar. A graph of  $I/I_0$  is shown in Figure 35, which clearly shows that the 6.5 microns of mylar effectively filtered the x-rays below approximately 1 keV. If the soft x-rays were dominated by energies of 1 keV and below, the energy collected by the optics with the mylar installed would be negligible compared to the optics without the mylar. In addition, the focal spot would be much wider due to the decreased reflectivity at higher energies. However, the optics with the mylar collected approximately 50% of the energy collected without the mylar and the focal spots are comparable. See Figures 25 and 26. Therefore it is concluded that the TR produced from the titanium foil stack was dominated by soft x-rays in the energy range of 1-3 keV and the original assumption of 2 keV is therefore valid.

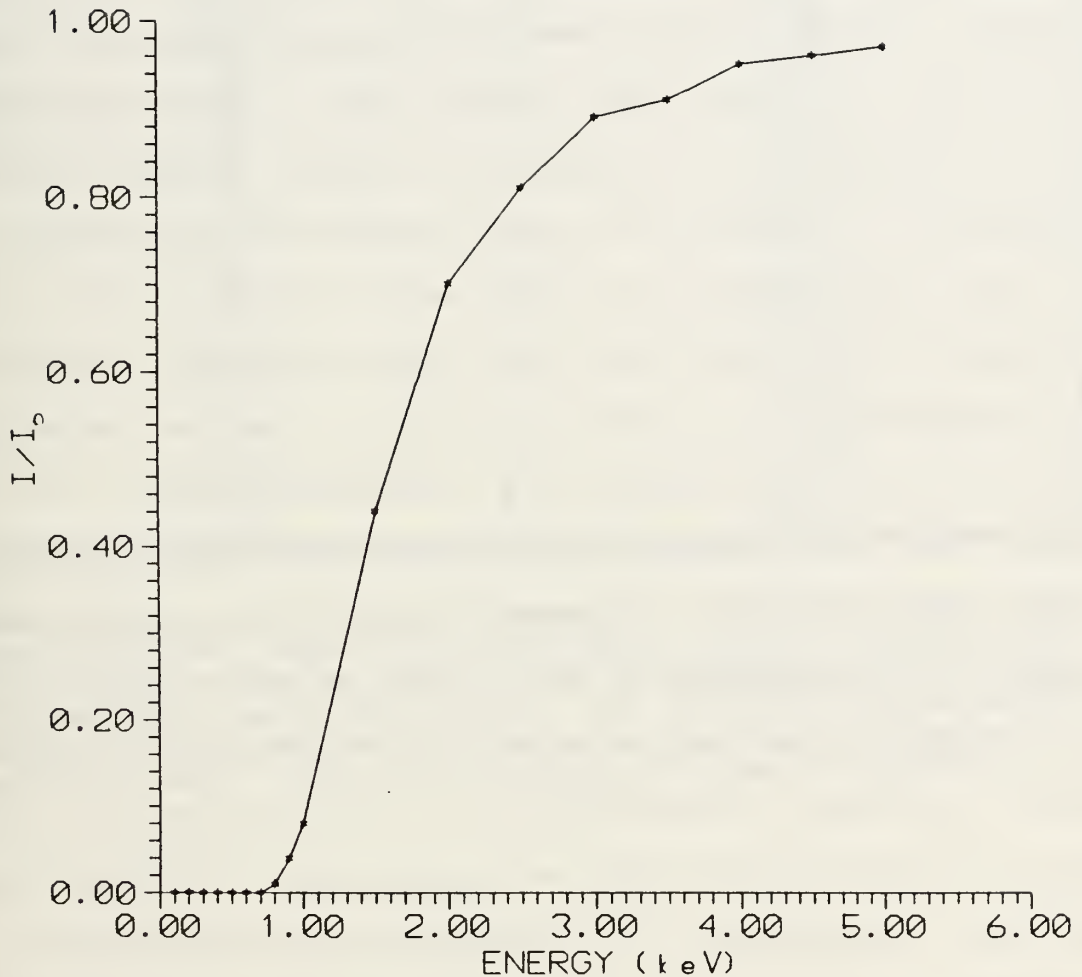


Figure 35. Attenuation of soft x-rays due to 6.5  $\mu\text{m}$  mylar covering the entrance of the optics.

Although superior performance of the nickel elliptical optic, with equivalent surface roughness at specific energies of soft x-rays has been shown, it is informative to investigate the performance of the nickel elliptical optic with equivalent surface roughness over a range of soft x-ray energies. Tables VI-VIII summarize the performance from .248 nm (5 keV) to 2.48 nm (500 eV) for each of the comparisons made. Figures 36-38 graphically display Tables VI-VIII respectively. Figures 39-41 are a graphical representation of the flux collected by the nickel optic divided by the flux collected by the quartz optic over the same energy range for each comparison. It is easily seen that as long as the energy of the x-rays was dominated by wavelengths below 1.24 nm (above 1 keV) the nickel elliptical optic performed as well or better than the quartz cylindrical optic. It was previously shown, in the discussion of the effects of mylar, that x-rays below 1 keV can be neglected with the titanium foil stack. However, they must be considered with the aluminum foil stack since a lower limit on x-ray energy was never determined for aluminum. Furthermore, it is unlikely that x-rays below 0.4 nm (above 3 keV) were dominant with either foil stack since the reflectivity of both optics goes to zero at this level.

TABLE VI

WAVELENGTH (nm)	CORRECTED FLUX COLLECTED (+/- 3.5 mm of peak) (J/coulomb)
2.48	0.20
2.38	0.21
2.28	0.21
2.18	0.22
2.08	0.23
1.98	0.24
1.88	0.25
1.78	0.26
1.68	0.28
1.58	0.30
1.48	0.33
1.38	0.37
1.28	0.43
1.18	0.52
1.08	0.65
0.98	0.86
0.88	1.29
0.78	2.58
0.68	5.17
0.58	15.5

Table VI. In reference to Figure 24, corrected flux collected by nickel optic with equivalent surface roughness as quartz optic assuming that the TR is monochromatic at each wavelength in the first column. The flux was corrected by the same procedure shown in Table V. The flux collected by the quartz optic was .511 J/coulomb as shown in Table V.

TABLE VII

WAVELENGTH (nm)	CORRECTED FLUX COLLECTED (+/- 3.5 mm of peak) (J/coulomb)
2.48	1.48
2.38	1.49
2.28	1.51
2.18	1.53
2.08	1.55
1.98	1.56
1.88	1.60
1.78	1.64
1.68	1.68
1.58	1.73
1.48	1.80
1.38	1.87
1.28	1.99
1.18	2.11
1.08	2.33
0.98	2.61
0.88	3.09
0.78	3.91
0.68	5.32
0.58	8.87

Table VII. In reference to Figure 25, corrected flux collected by nickel optic with equivalent surface roughness as quartz optic assuming that the TR is monochromatic at each wavelength in the first column. The flux was corrected by the same procedure shown in Table V. The flux collected by the quartz optic was 2.04 J/coulomb as shown in Table V.

TABLE VIII

WAVELENGTH (nm)	CORRECTED FLUX COLLECTED (+/- 3.5 mm of peak) (J/coulomb)
2.48	0.72
2.38	0.73
2.28	0.74
2.18	0.75
2.08	0.76
1.98	0.77
1.88	0.78
1.78	0.80
1.68	0.82
1.58	0.86
1.48	0.88
1.38	0.93
1.28	0.97
1.18	1.05
1.08	1.16
0.98	1.30
0.88	1.55
0.78	1.97
0.68	2.71
0.58	4.64

Table VIII. In reference to Figure 26, corrected flux collected by nickel optic with equivalent surface roughness as quartz optic assuming that the TR is monochromatic at each wavelength in the first column. The flux was corrected by the same procedure shown in Table V. The flux collected by the quartz optic was 1.22 J/coulomb as shown in Table V.

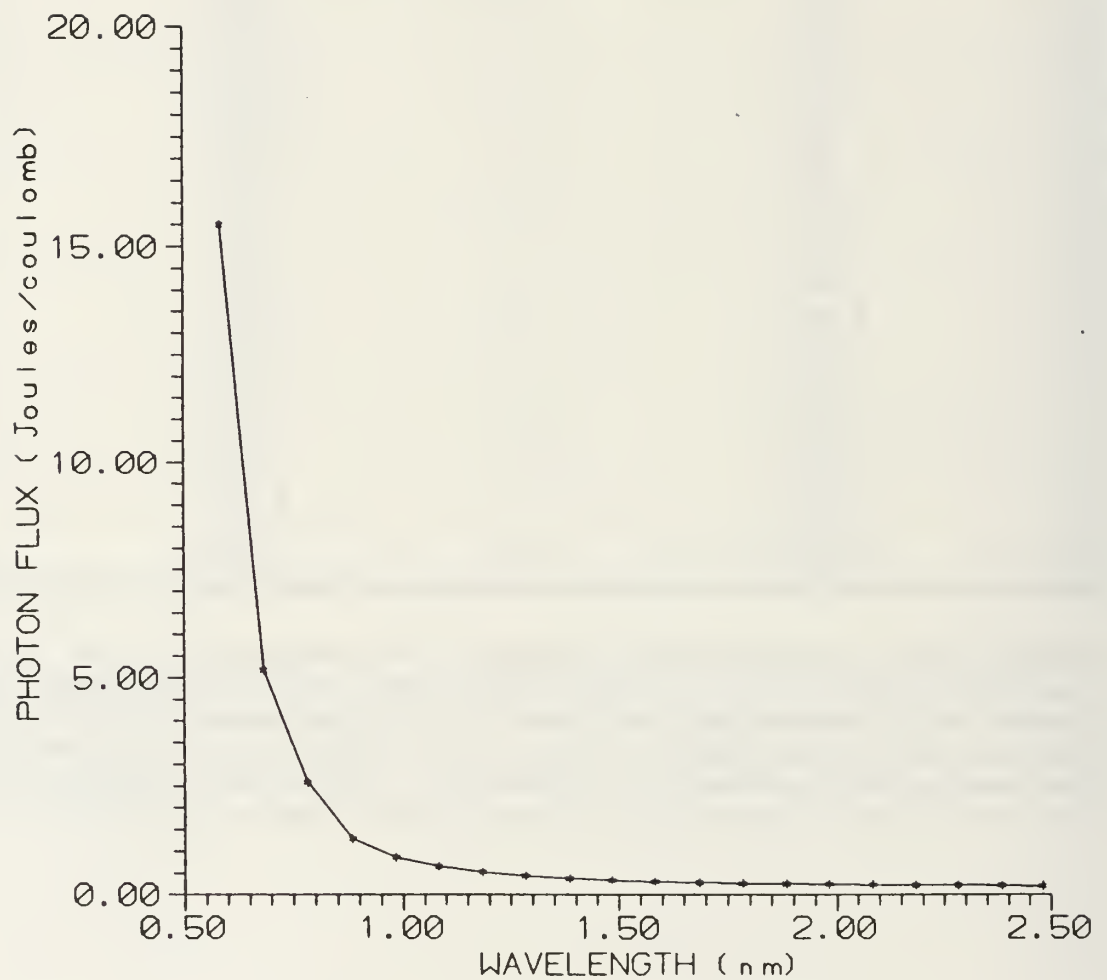


Figure 36. Graphical display of data in Table VI.

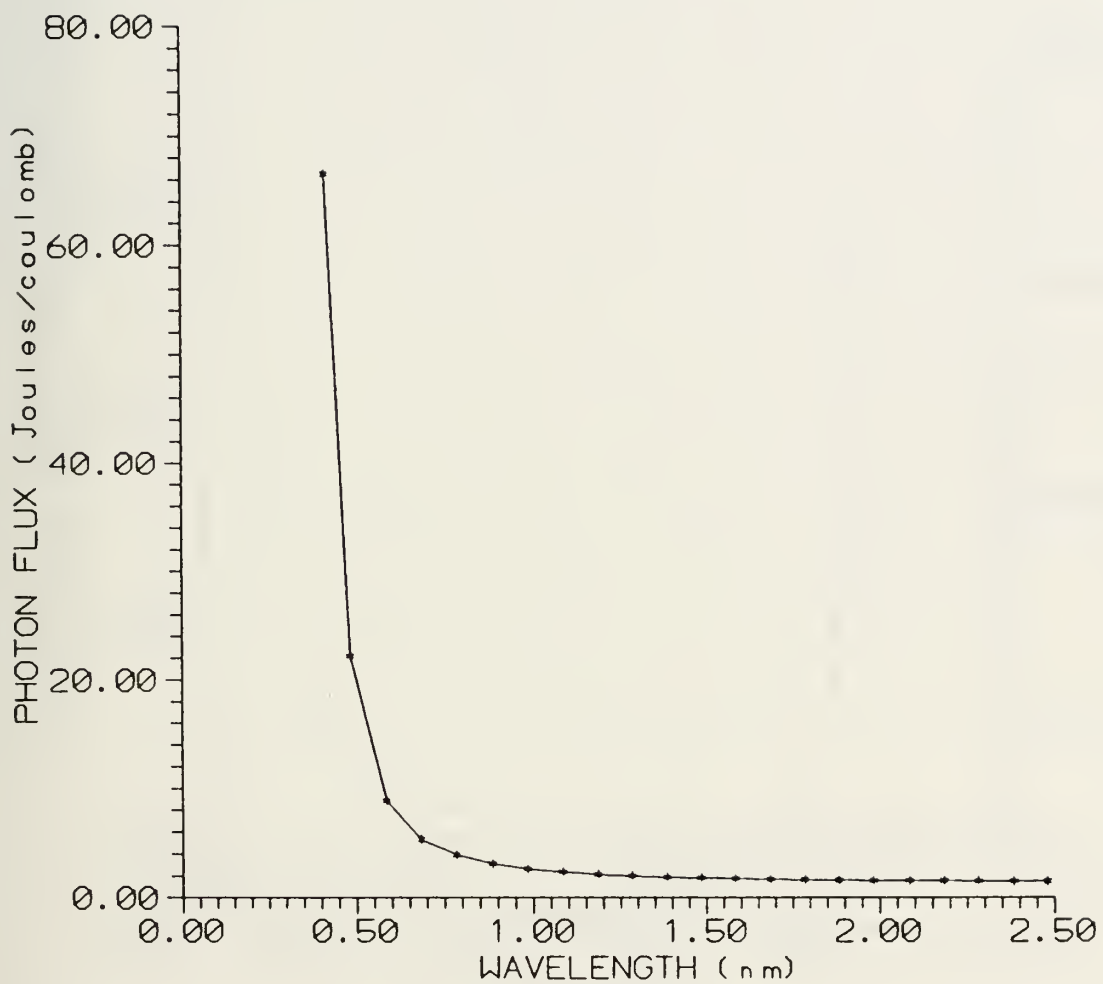


Figure 37. Graphical display of data in Table VII.

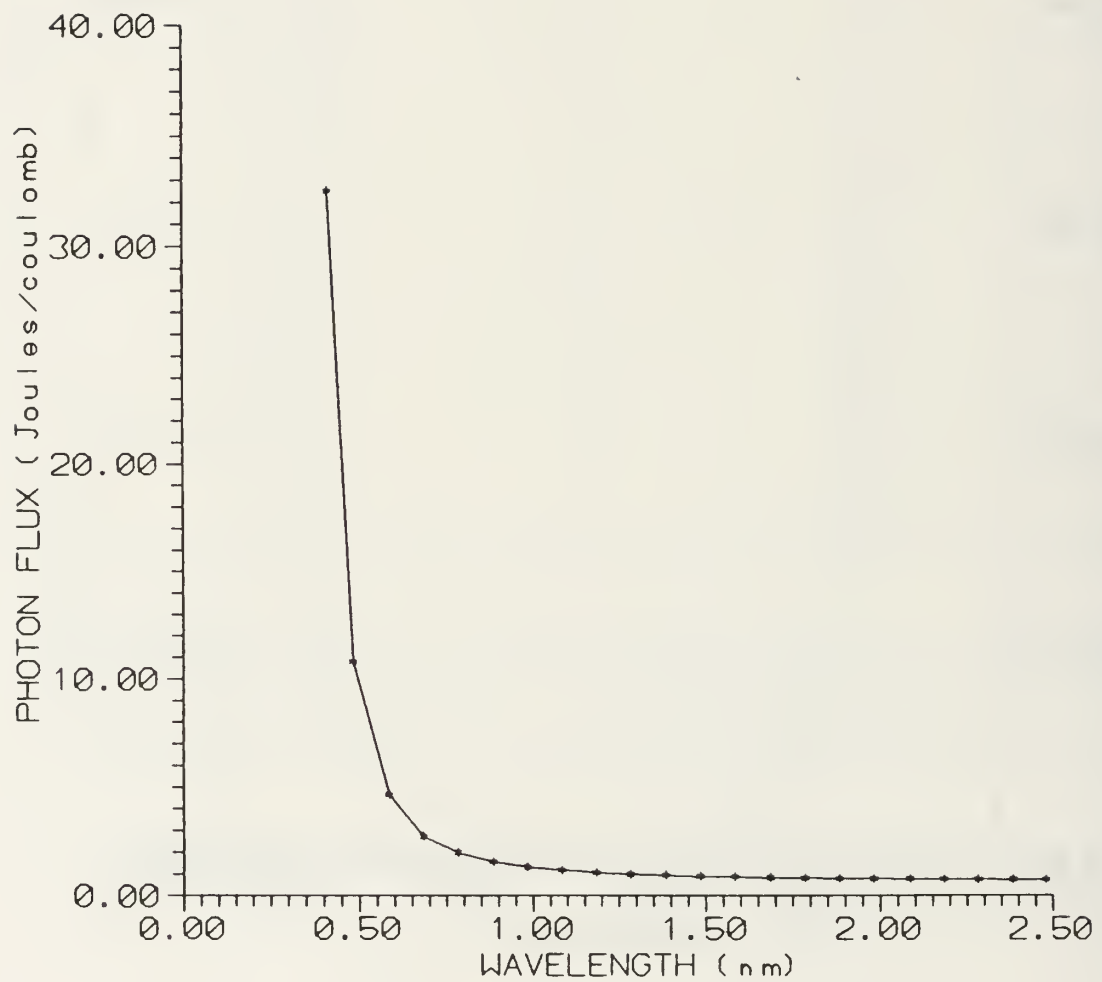


Figure 38. Graphical display of data in Table VIII.

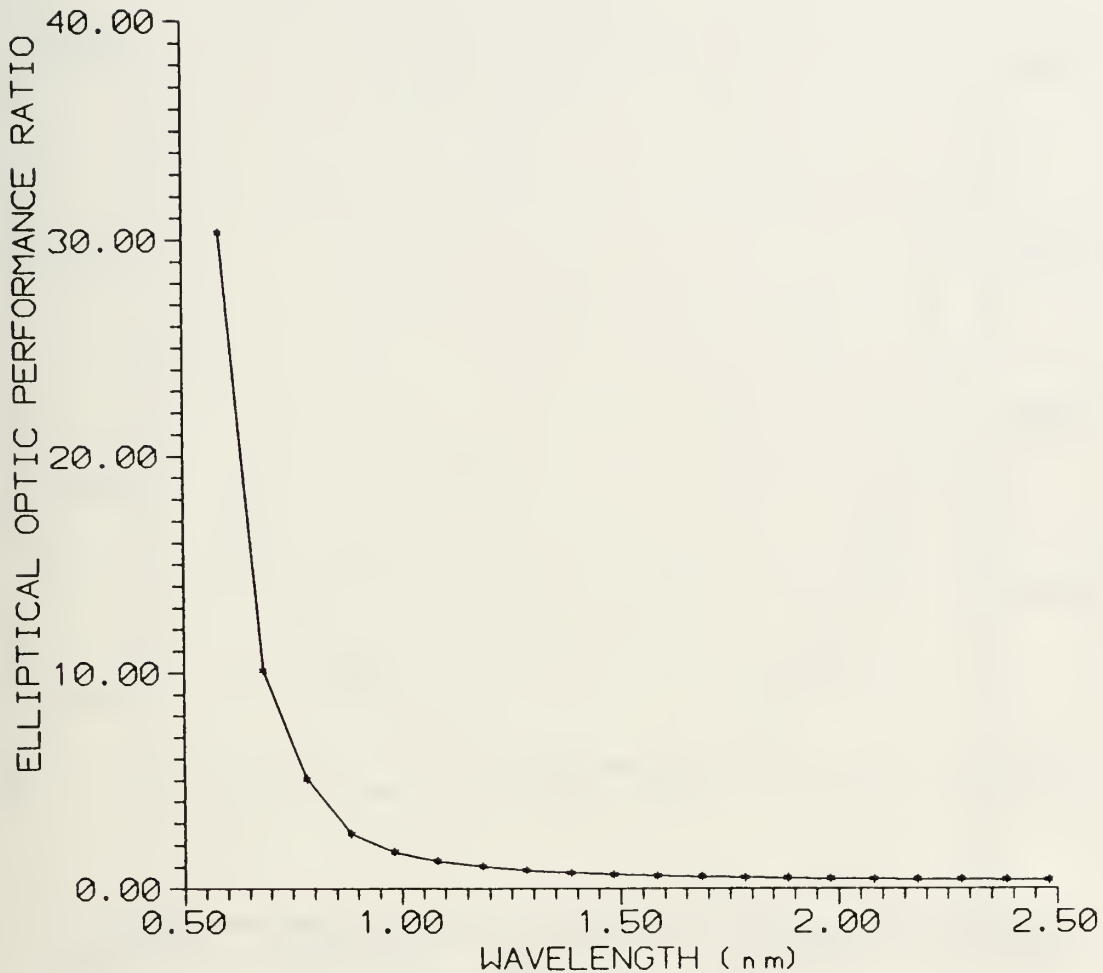


Figure 39. Graphical display of corrected flux, as given in Table VI, divided by the flux collected by the quartz optic as stated in the caption of Table VI. This graph is the same graph as in Figure 36, divided by .511 J/coulomb.

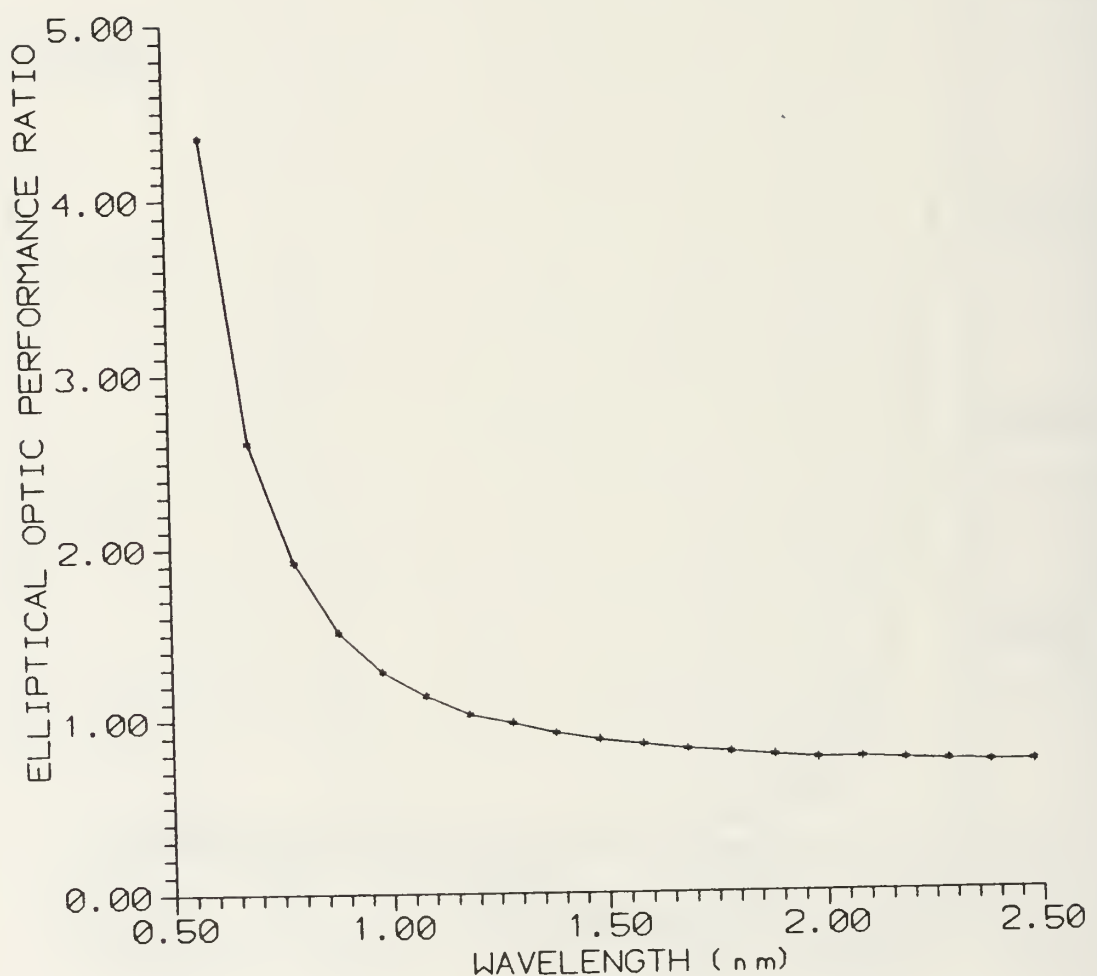


Figure 40. Graphical display of corrected flux, as given in Table VII, divided by the flux collected by the quartz optic as stated in the caption of Table VII. This graph is the same graph as in Figure 37, divided by 2.04 J/coulomb.

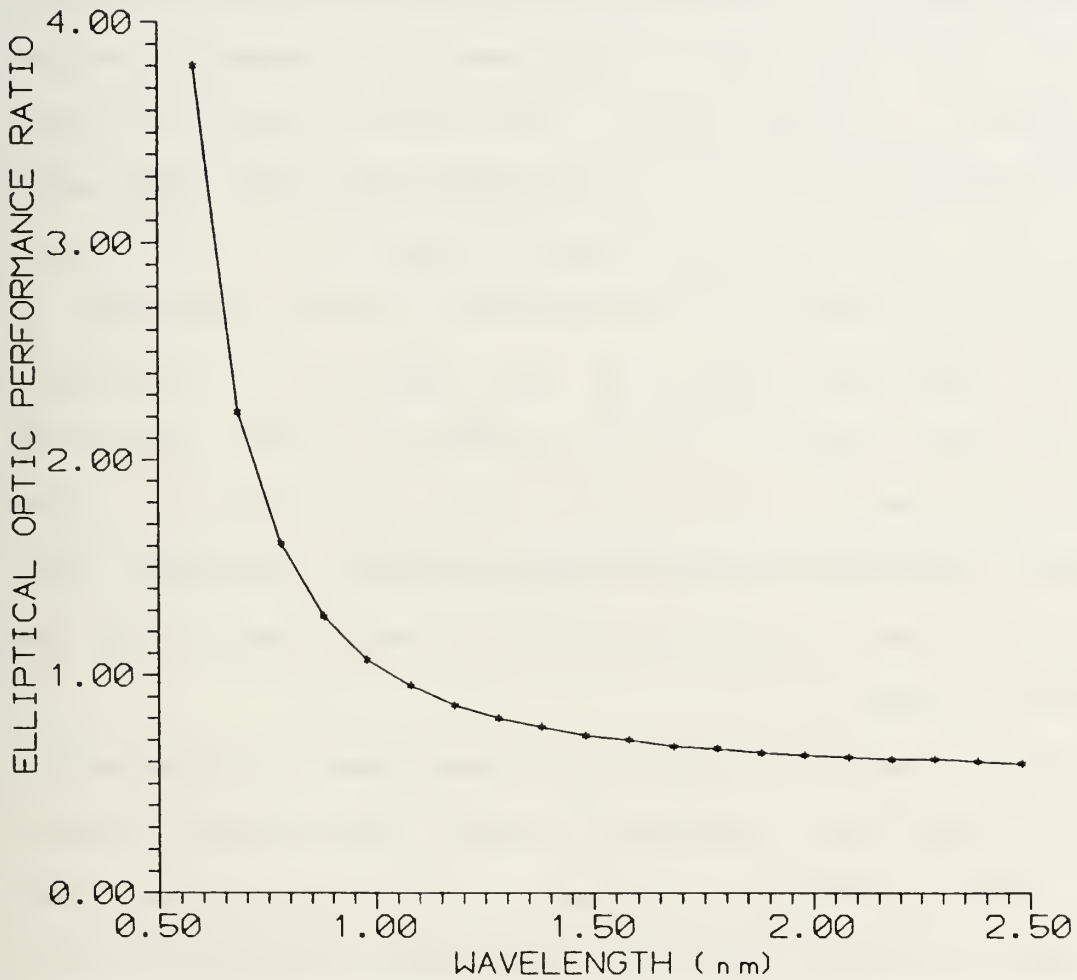


Figure 41. Graphical display of corrected flux, as given in Table VIII, divided by the flux collected by the quartz optic as stated in the caption of Table VIII. This graph is the same graph as in Figure 38, divided by 1.22 J/coulomb.

## VI. CONCLUSIONS AND RECOMMENDATIONS

A cylindrical or elliptical optic coupled to a transition radiation x-ray source is a viable and practical method of focusing x-rays. If the transition radiation is dominated by 1-3 keV x-rays, the nickel elliptical optic demonstrates the possibility of collecting 3-5 times more energy than the quartz cylindrical optic. The peak height and FWHM were better with the cylindrical quartz optic due to the nickel elliptical optic having a much greater surface roughness. A follow up experiment should be done comparing a cylindrical and elliptical optic of the same material with equivalent surface roughness. This would allow the effect of the different geometries to be analyzed directly. Adelphi Tech. has recently had a nickel cylindrical optic fabricated for just this purpose.

In carrying out this follow on experiment it is essential that the optics are concentric to the axis of the conical photon beam as defined by the axis of the electron beam, and that they are placed exactly at the midpoint between the foil stack and detector. This will ensure maximum reflection and minimize the FWHM at focus.

The theory behind the elliptical optical focusing system assumes a point source. Since the TR produced is not a true

point source, there will be some inherent focal spreading. It might be worth considering using the flash x-ray machine to overcome this effect.

## LIST OF REFERENCES

1. Jackson, J.D., *Classical Electrodynamics*, pp. 685-693, Wiley, New York, 1962.
2. Cherry, M.L., Muller, D., and Prince, T.A., "Transition Radiation from Relativistic Electrons in Periodic Radiators," *Physics Review D.*, Vol. 10, pp. 3594-3607, Dec. 1974.
3. Chu, A.N., Piestrup, M.A., Pantell, R.H., and Buskirk, F.R., "Soft X-Ray Production from Transition Radiation Using Thin Foils," *Journal of Applied Physics*, Vol. 52., p. 22, 1981.
4. Reitz, J.R., Milford, F.J., and Christy, R.W., *Foundations of Electromagnetic Theory*, P. 285, Addison-Wesley, California, 1967.
5. Chung, P.S., and Pantell, R.H., *Electronics Letters*, Vol. B, p. 527, 1977.
6. Piestrup, M.A., and others, "Transition Radiation as an X-Ray Source for Lithography," *Electron Beam, X-Ray and Ion-Beam Lithographies VI*, SPIE Vol. 773, 1987.
7. Pantell, R.H., and Chung, P.S., *IEEE J. Quant. Electr.*, Vol. QE-14, p. 694, 1978.
8. Mosner, D., and Stephanakis, S.J., *Applied Physics Letters*, Vol. 29, p. 105, 1976.
9. Michette, A.G., *Optical Systems for Soft X-Rays*, pp. 37-53, Plenum, New York, 1986.
10. *Handbook of Optical Constants*, edited by E.D. Palik, Academic Press Inc., 1985.
11. Berkey, D.D., *Calculus*, pp. 616-617, Saunders College, New York, 1988.
12. Surface Roughness Tests conducted by Jack Harris, Adelphi Tech. Inc., private communications, July 1991.

13. Hamamatsu Linear Image Detector Specifications, Model S2301.
14. E G & G Reticon Appl. Notes #100, Application of Reticon Photon Diode Arrays as Electron and X-Ray Detectors, EIG 5, 1975.
15. Conners, S.M., Effects of High Energy Electron Irradiation on a  $YB_2Cu_3O_7$ , High Temperature Superconductor, Master's Thesis, Naval Postgraduate School, Monterey, California, September 1991.
16. Piestrup, M.A., and others, "Quasimonochromatic X-Ray Source Using Photoabsorption-edge Transition Radiation," Physics Rev. Letters, December 1990.
17. Piestrup, M.A., and others, "High Power X-Ray Generation Using Transition Radiation," Physics Rev. A43, pp. 2387-2396, 1990.
18. Krane, K.S., Introductory Nuclear Physics, pp. 198-204, Wiley, New York, 1988.
19. Fisher, P.C., Humphreys, C.L., and Roethig, D.T., "X-Ray Attenuation Coefficients of Some Low Z Elements," LMSC 6-74-64-3, Lockheed Missile and Space Co. Research Laboratory, Palo Alto, California, January 1964.
20. Kumakhov, M.A., "Channeling of Photons and New X-Ray Optics," Nuclear Instruments and Methods in Physics Research B48, pp. 283-286, North-Holland, 1986.
21. Amato, Ivan, "Piping X-Rays Through a Glass Brightly," Science Magazine, Vol. 252, pp. 208-209, 12 April 1991.

## APPENDIX A

### A. ALTERNATIVE X-RAY OPTICS

An alternative method of focusing x-ray transition radiation was studied by M. A. Kumakhov of the Soviet Union in 1986 [Ref. 19]. The use of optical grazing incidence, based on the effect of total external reflection, is also the theory behind this study. He proposed the development of x-ray optics based on multiple reflection of x-ray radiation from suitably curved surfaces. The various x-ray optical systems created on this basis allow the handling of x-ray beams with a wide range of frequencies and angles. The energy interval that was examined was between 0.1 keV to 10 MeV, i.e., the x- and gamma-ray range. The angles were varied from a few to several hundred times the angle of total external reflection; e.g., at photon energies of keV these angles are of the order of 1-2 rad.

These new optics make it possible to concentrate extremely high densities of x-ray radiation in a small spot on an object under investigation. In addition, these optics allow one to form a quasiparallel beam of large cross section from a high divergence beam.

The optics are illustrated in Figure A-1. Assuming that an x-ray photon is reflected from a surface with a high

probability (close to unity) it can travel along an empty channel while being reflected many times. If this channel is curved so that the radius of curvature:

$$R > \frac{d}{\theta_k^2}$$

where  $d$  is the diameter of the channel and  $\theta_k$  is the Fresnel reflection angle, the photon will travel in the curved channel. In order transform radiation with divergence into a parallel beam, the geometry illustrated in Figure A-2 is required. The angle of divergence is divided into smaller angles and each curved channel turns by a required angle that part of the radiation which enters the channel. A channel on the periphery obviously will turn radiation by a larger angle than a channel located near the axis. The channels, a system of layered smoothly curved capillary tubes, were arranged so that the angles of incidence on the channel walls were smaller than the Fresnel reflection angle. This system made it possible to transform divergent radiation into an almost parallel beam. Figure A-3 illustrates an extension of this geometry where x-ray lens not only transforms divergent radiation into a parallel beam, but further focuses it in a required spot.

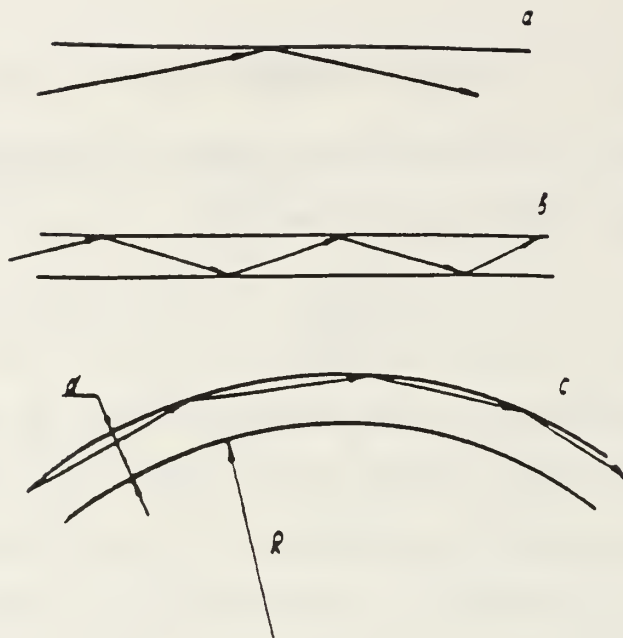


Figure A-1. Illustration of "channeling" of photons.

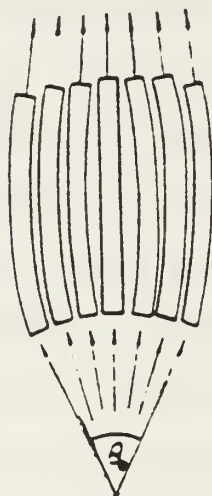


Figure A-2. Illustration of the transformation of a divergent into a quasiparallel beam.

A photograph of the first x-ray lens made in the Soviet Union is presented in Figure A-4. The angle of radiation capture is  $23^\circ$ , the focal length is 5 cm, and the total length of the lens is 98 cm. It consists of 2000 capillary tubes with an outer diameter of 0.4 mm and a channel diameter of 0.36 mm. The capillary tubes form a hexagonal close-packed array in cross section. The area of the hollow channels cover 73% of the total area of the entry and exit cone of the system. The length of the end linear section of the capillary tubes is 5 cm. The middle section of the capillary tubes has a radius of curvature ranging from two meters in the outer layer to infinity for the central tube. The lens was designed for focusing soft x-rays (1-2 keV). Figure A-5 shows x-ray photographs taken at different distances from the exit cone of the system. It can be seen very clearly how 2,000 x-ray beams are focused at an exactly calculated distance. Figure A-6 is a photograph of a system that transforms divergent radiation into a quasiparallel beam. It is an x-ray lens truncated in its middle. It consists of 12,000 capillary tubes, and it transforms radiation with a divergence of 0.5 rad into a quasiparallel beam with a divergence of  $10^{-2}$  rad. The cross sectional area of the beam is approximately  $200 \text{ cm}^2$ .

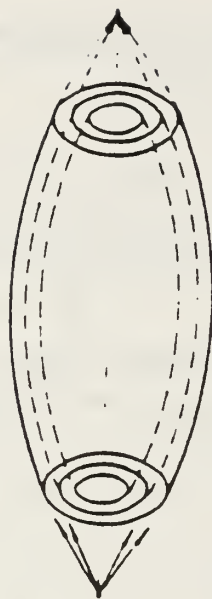


Figure A-3. Illustration of the geometry for an x-ray lens.

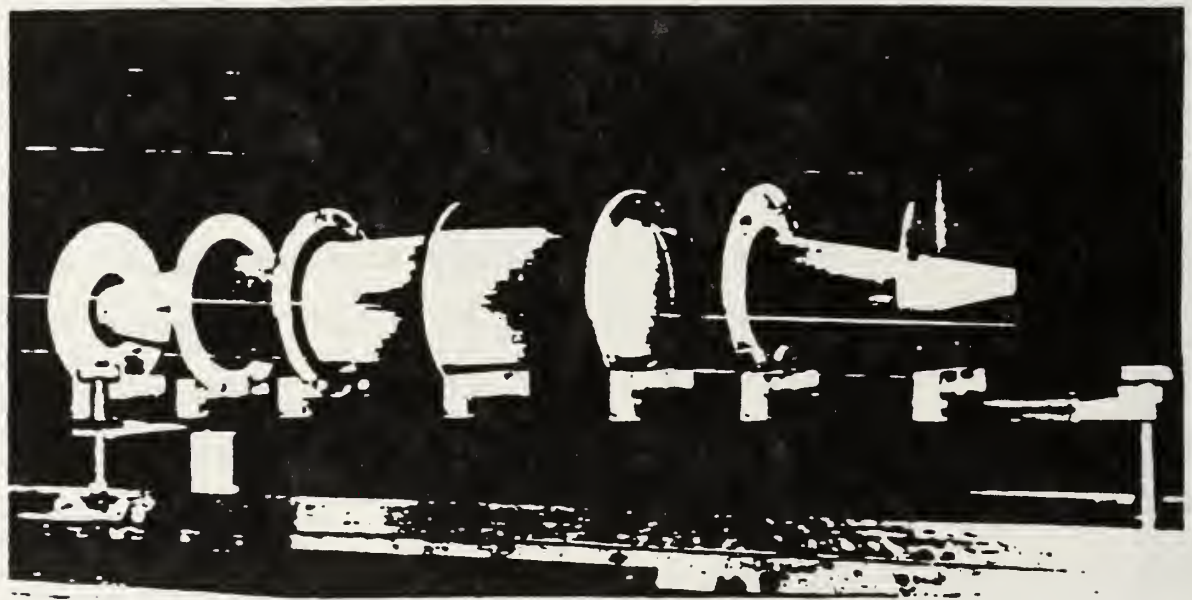


Figure A-4. Photograph of an x-ray lens.

The results obtained from these experiments show promising application for these optical systems. They can be used in combination with sources such as high-power x-ray tubes, laser-plasma and pinch x-ray sources, synchrotron radiation, channeling radiation, and transition radiation. In 1990, Walter Gibson, a highly regarded physicist from the State University of New York at Albany, founded a company called X-Ray Optical Systems Inc., with the goal of marketing the Kumakhov Lens [Ref. 20].

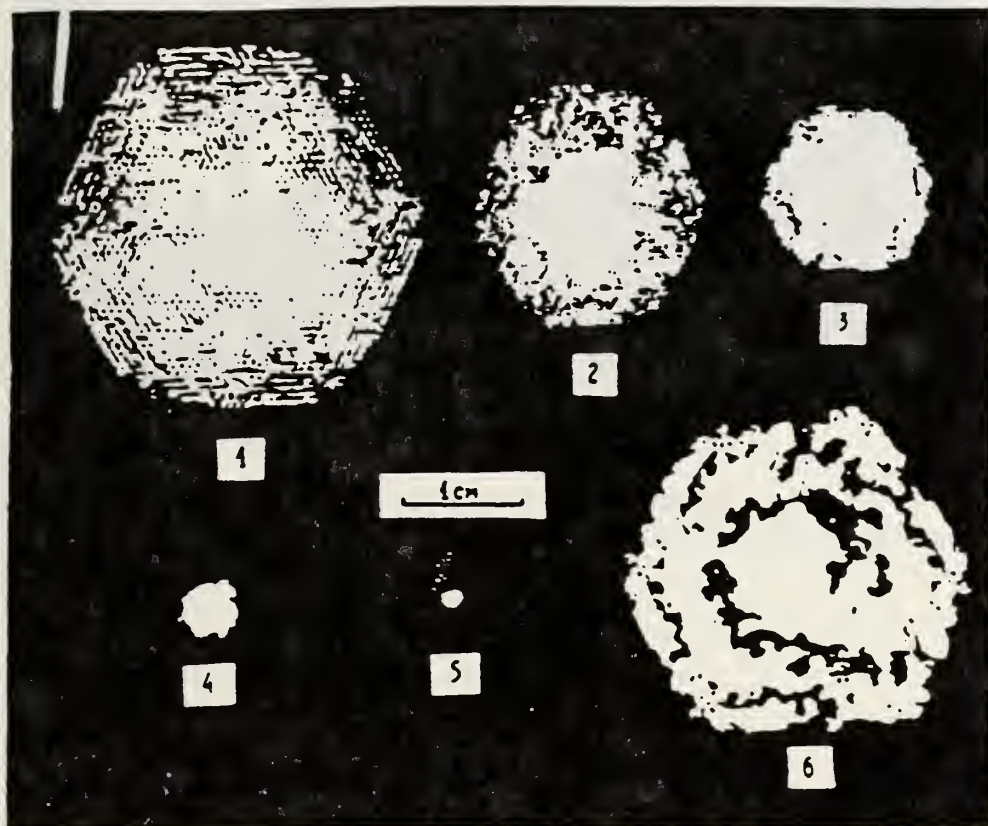


Figure A-5. Process of focusing 2,000 x-ray beams.

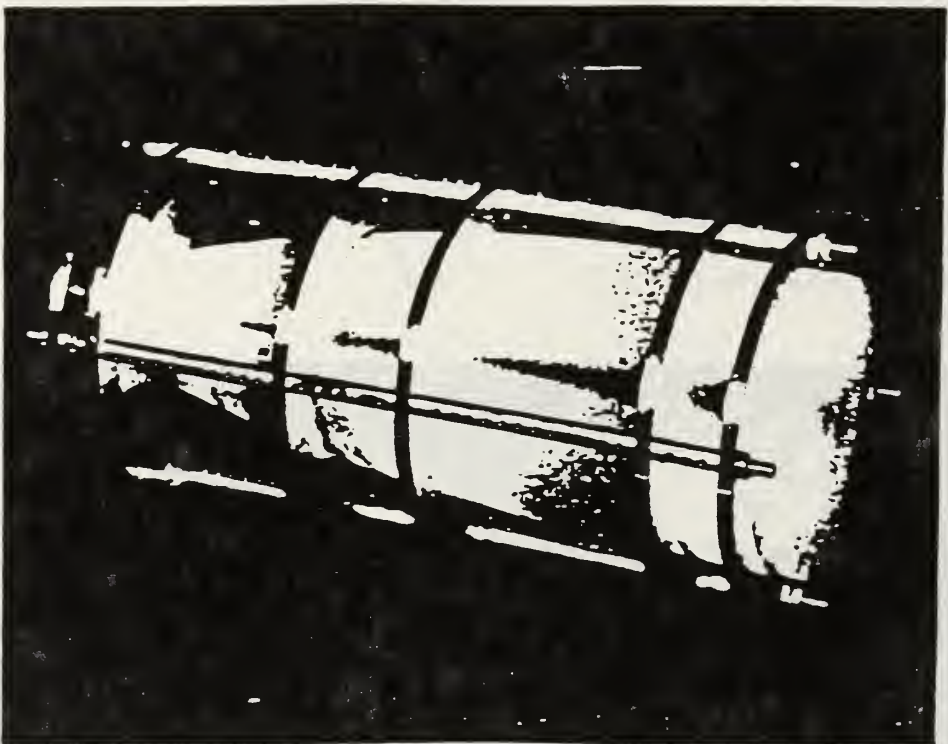


Figure A-6. X-ray system for transformation of a divergent into a quasiparallel beam.

## INITIAL DISTRIBUTION LIST

1.	Defense Technical Information Center Cameron Station Alexandria, Virginia 22304-6145	2
2.	Library, Code 52 Naval Postgraduate School Monterey, California 93943-5002	2
3.	Dr. K.E. Woehler, Code Ph/Wh Department of Physics Naval Postgraduate School Monterey, California 93943-5002	1
4.	Professor X.K. Maruyama, Code Ph/Mx Department of Physics Naval Postgraduate School Monterey, California 93943-5002	3
5.	Lt. Paul M. Votruba, USN 8600 Hastings St. N.E. Blaine, Minnesota 55434	1
6.	Professor F.E. Buskirk, Code Ph/Nb Department of Physics Naval Postgraduate School Monterey, California 93943-5002	1
7.	Professor J.R. Neighbours, Code Ph/Nb Department of Physics Naval Postgraduate School Monterey, California 93943-5002	1
8.	Dr. M.A. Piestrup Adelphi Technology, Inc. 532 Emerson Street Palo Alto, California 94301	1
9.	Mr. H. Reitdyk, Code Ph Department of Physics Naval Postgraduate School Monterey, California 93943-5002	2

10. Mr. R. Carlson, Code M-4  
Los Alamos National Laboratory  
Post Office Box 1663  
Los Alamos, New Mexico 87545

1

845-216





Thesis  
V98348  
c.1

Thesis  
V98348  
c.1

Votruba  
Focusing transition  
radiation with cylindri-  
cal and elliptical optics.

Thesis  
V98348 Votruba  
c.1 Focusing transition  
radiation with cylindri-  
cal and elliptical optics.





3 2768 00018435 2